Mon. Not. R. Astron. Soc. **399,** 1447–1470 (2009) doi:10.1111/j.1365-2966.2009.15368.x

The H I gas content of galaxies around Abell 370, a galaxy cluster at $z = 0.37$

Philip Lah,[1⋆] Michael B. Pracy,[1] Jayaram N. Chengalur,[2] Frank H. Briggs,[1] Matthew Colless,[3] Roberto De Propris,[4] Shaun Ferris,[1] Brian P. Schmidt[1] and Bradley E. Tucker[1]

[1]*Research School of Astronomy and Astrophysics, The Australian National University, Weston Creek, ACT 2611, Australia*
[2]*National Centre for Radio Astrophysics, Post Bag 3, Ganeshkhind, Pune 411 007, India*
[3]*Anglo-Australian Observatory, PO Box 296, Epping, NSW 2111, Australia*
[4]*Cerro Tololo Inter-American Observatory, Casilla 603, La Serena, Chile*

Accepted 2009 July 6. Received 2009 July 3; in original form 2008 November 3

ABSTRACT

We used observations from the Giant Metrewave Radio Telescope to measure the atomic hydrogen gas content of 324 galaxies around the galaxy cluster Abell 370 at a redshift of $z = 0.37$ (a look-back time of ∼4 billion years). The H I 21 cm emission from these galaxies was measured by co-adding their signals using precise optical redshifts obtained with the Anglo-Australian Telescope. The average H I mass measured for all 324 galaxies is $(6.6 \pm 3.5) \times 10^9\,M_\odot$, while the average H I mass measured for the 105 optically blue galaxies is $(19.0 \pm 6.5) \times 10^9\,M_\odot$. The significant quantities of gas found around Abell 370 suggest that there has been substantial evolution in the gas content of galaxy clusters since redshift $z = 0.37$. The total amount of atomic hydrogen gas found around Abell 370 is up to approximately eight times more than that seen around the Coma cluster, a nearby galaxy cluster of similar size. Despite this higher gas content, Abell 370 shows the same trend as nearby clusters that galaxies close to the cluster core have lower H I gas content than galaxies further away where the galaxy density is lower. The optically blue galaxies contain the majority of the H I gas surrounding the cluster. However, there is evidence that the optically red galaxies contain appreciable quantities of H I gas within their central regions. The Abell 370 galaxies have H I mass-to-optical-light ratios similar to local galaxy samples and have the same correlation between their star formation rate and H I mass as found in the nearby galaxies. The average star formation rate derived from [O II] emission and from deredshifted 1.4 GHz radio continuum for the Abell 370 galaxies also follows the correlation found in the local Universe. The large amounts of H I gas found around the cluster can easily be consumed entirely by the observed star formation rate in the galaxies over ∼4 billion years (from $z = 0.37$) to the present day. Abell 370 appears set to evolve into a gas-poor system similar to galaxy clusters observed in the local Universe.

Key words: galaxies: evolution – galaxies: ISM – radio continuum: galaxies – radio lines: galaxies.

1 INTRODUCTION

Galaxy properties, such as morphology and star formation rate (SFR), are found to depend on environmental density. These effects probably originate from a density-dependent quenching of star formation which can come about via the consumption or removal of the available gas supply in the galaxies. As such the amount of H I gas available to galaxies to fuel further star formation is likely to be a fundamental parameter in understanding the effect of environment. Galaxies in nearby clusters and their surroundings show strong evidence for environmental effects on their gas content. However, at higher redshifts the gas content of clusters has not been studied in detail. Consequently, our understanding of the effect of environment on galaxy evolution has been incomplete.

As the number density of galaxies increases, the rate of star formation in the galaxies decreases. This star formation–density correlation can be seen locally in the variation of the fraction

⋆E-mail: plah@mso.anu.edu.au

of blue galaxies with galaxy density (Pimbblet et al. 2002; De Propris et al. 2004) and in the fraction of emission line galaxies with galaxy density (Hashimoto et al. 1998; Lewis et al. 2002; Gómez et al. 2003; Balogh et al. 2004; Kauffmann et al. 2004). At higher redshift, the blue fraction of galaxies in the dense environment of clusters increases with redshift (Butcher & Oemler 1984) as does the fraction of galaxies with emission lines (Couch & Sharples 1987; Balogh et al. 1998, 1999; Poggianti et al. 1999; Dressler et al. 2004). The amount of star formation in galaxies in general increases with redshift, with there being an order of magnitude increase in the cosmic SFR density between the present time and $z \sim 1$ (Lilly et al. 1996; Madau et al. 1996; Hopkins 2004). The trend that with higher galaxy density there are fewer galaxies with ongoing star formation continues to at least $z \sim 0.8$ (Poggianti et al. 2008).

In the local Universe, the proportion of galaxies which are ellipticals or S0 galaxies increases with galaxy number density, and there is a corresponding decrease in spirals galaxies (Dressler 1980). This density–morphology relationship also evolves with redshift. While the fraction of elliptical galaxies in dense cluster environments stays reasonably constant, the fraction of S0 galaxies decreases from present values by a factor of 2–3 by $z \sim 0.5$ and there is a proportional increase in the spiral galaxy fraction at the same time (Dressler et al. 1997; Fasano et al. 2000).

The physical mechanisms considered when attempting to understand these environment trends all involve processes that affect the gas content of the galaxies, the fuel supply for star formation. These proposed physical mechanisms include the following.

(i) Galaxy mergers and strong gravitational galaxy–galaxy interactions (Toomre & Toomre 1972).

(ii) Galaxy harassment, which is the cumulative effect of tidal forces from many weak galaxy encounters (Richstone 1976; Farouki & Shapiro 1981; Moore et al. 1996; Moore, Lake & Katz 1998).

(iii) Interactions between a galaxy and the intergalactic medium (IGM), which includes ram pressure stripping, viscous stripping and thermal evaporation (Gunn & Gott 1972; Quilis, Moore & Bower 2000).

(iv) Strangulation, which is the removal of any envelope of hot gas surrounding galaxies that was destined to cool and accrete on to the galaxy to fuel further star formation (Larson, Tinsley & Caldwell 1980; Diaferio et al. 2001).

These mechanisms affect the gas either by stimulating star formation (which rapidly consumes the gas, locking it up in stars) or by removing the gas from the galaxy (and ionizing it) or by preventing further accretion. Unlike the other mechanisms listed which quench star formation relatively quickly ($\sim 10^7$ years), strangulation causes a slow decline in star formation over longer time-scales (>1 Gyr) (Poggianti 2004).

Neutral atomic hydrogen gas (H I) is a large component of the gas content of galaxies and can be directly quantified from H I 21 cm emission. In the central regions of nearby clusters, late-type galaxies are found to be H I deficient compared to similar galaxies in the field (Haynes, Giovanelli & Chincarini 1984). This effect continues well outside the cluster cores with a gradual change in the H I content of galaxies with galaxy density (Solanes et al. 2001). Galaxies in nearby clusters show evidence of disruption of their H I gas with the presence of unusual asymmetric H I gas distributions, spatial offsets between the H I and optical discs, and tails of H I gas streaming away from the galaxies (Cayatte et al. 1990; Bravo-Alfaro et al. 2000; Chung et al. 2007). Despite these gas depletion trends with galaxy number density in the local Universe, the high H I mass galaxies are found to trace the same galaxy densities as the optical galaxies while the low H I mass galaxies trace low-density environments (Basilakos et al. 2007). This pattern is likely to continue at higher redshift making the search for high H I mass galaxies easier around optical overdensities of galaxies.

Observing H I 21 cm emission from galaxies at cosmological distances ($z > 0.1$) is difficult due to the weak flux of the line. Only a single galaxy with H I 21 cm emission was detected in the rich cluster Abell 2218 at $z = 0.18$ using 216 hours with the Westerbork Synthesis Radio Telescope (WSRT) (Zwaan, van Dokkum & Verheijen 2001). Again only a single galaxy with H I 21 cm emission was detected in the galaxy cluster Abell 2192 at $z = 0.19$ using $\sim$80 hours with the Very Large Array (VLA) (Verheijen 2004). After an upgrade of the WSRT, a new pilot study was able to detect H I 21 cm emission from 19 galaxies in Abell 963 at $z = 0.21$ using 240 hours and 23 galaxies in Abell 2192 at $z = 0.19$ using 180 hours (Verheijen et al. 2007). Additionally, the upgraded Arecibo radio telescope has detected H I 21 cm emission at redshifts between $z = 0.17$ and 0.25 from $\sim$20 isolated galaxies selected in the optical from the Sloan Digital Sky Survey (Catinella et al. 2008). While the number of H I 21 cm emission galaxies directly detected at cosmological distances has been increasing with time, the number is still small and limited to the most gas-rich systems.

To quantify the H I gas content of large numbers of galaxies at cosmologically interesting redshifts, we have been co-adding the H I 21 cm emission from multiple galaxies using their observed optical positions and redshifts. The co-adding technique for measuring neutral atomic hydrogen gas has been used previously in galaxy cluster Abell 2218 at $z = 0.18$ (Zwaan 2000) and in Abell 3128 at $z = 0.06$ (Chengalur, Braun & Wieringa 2001). We expanded this technique to field galaxies with active star formation at $z = 0.24$ (Lah et al. 2007).

The goal of this work is to quantify the evolution of the H I gas in galaxies in a variety of environments. At moderate redshifts, the angular extent of galaxy clusters is sufficiently small enough that galaxy environments from the dense cluster core to almost field galaxy densities can be observed in a single radio telescope pointing. In this paper, we are applying the H I co-adding technique to galaxies surrounding Abell 370, a galaxy cluster at $z = 0.37$ (a look-back time of $\sim$4.0 billion years). Abell 370 is a large galaxy cluster, similar in size and mass to the nearby Coma cluster. The H I gas content of galaxies at different distances from the Abell 370 cluster core is examined, in particular that of galaxies inside and outside the extent of the hot, X-ray emitting, intracluster gas as well as that of galaxies inside and outside the cluster R_{200} radius (the radius at which the galaxy density is 200 times the general field).

In this paper, the cluster centre of Abell 370 has been set as the mid-point between the two cD galaxies which is at right ascension (RA) $02^{\rm h}39^{\rm m}52\overset{\rm s}{.}90$ declination (Dec.) $-01^\circ 34' 37\overset{''}{.}5$ J2000. This value is close to the centre determined from X-ray measurements (Ota & Mitsuda 2004), and a good match to the velocity and surface density distribution of the galaxy data used in this paper. The redshift of the cluster centre has been set as $z = 0.373$ based on the galaxy redshift distribution we observed. The observations used in this paper are listed in Table 1.

We adopt the consensus cosmological parameters of $\Omega_\lambda = 0.7$, $\Omega_{\rm M} = 0.3$ and $H_0 = 70\ {\rm km\,s^{-1}\,Mpc^{-1}}$ throughout this paper.

The structure of this paper is as follows. Section 2 details the optical imaging and optical spectroscopy of the Abell 370 galaxies. Section 3 details the radio observations and data reduction. Section 4 presents the measurement of the H I 21 cm emission signal from all the Abell 370 galaxies with usable redshifts. Section 5 presents the H I signal from different subsamples of these galaxies. Section 6

Table 1. List of telescope observations used in this paper.

Telescope	Type of observation	Date of observations	Duration of observations
GMRT	Radio spectroscopy	2003 August 10–17	63 h
ANU 40 inch	Optical imaging	2005 November 1 and 2	2 nights
ANU 40 inch	Optical imaging	2006 September 19–24	5 nights
AAT	Optical spectroscopy	2006 October 11–14	4 nights

details the comparison of the H I results for Abell 370 with various literature measurements. Section 7 elaborates on the star formation properties of the Abell 370 galaxies. Finally, Section 8 presents a summary and discussion of the results.

2 THE OPTICAL DATA

2.1 The optical imaging and galaxy target selection

Wide-field and moderately deep imaging of the galaxy cluster Abell 370 and its surroundings were obtained using the WFI on the Australian National University (ANU) 40-inch telescope at the Siding Spring Observatory. There were two separate observing runs: the first on 2005 November 1 and 2, and the second on 2006 September 19–24. Both sets of observations were taken through the standard broad passband filters V, R and I.

The WFI has a 52 × 52 arcmin field of view which is sampled by a mosaic of eight 2 k × 4 k CCDs. One of these detectors was not functioning leaving a 12 arcmin × 24 arcmin gap in the imaged field. In 2005 November, only a single WFI pointing was observed, leaving in a gap in the imaging due to the missing CCD. The conditions during this run were close to photometric and the seeing in the final combined imaging was ∼2.1 arcsec. The average 3σ surface brightness limit of this imaging was 25.5 mag arcsec^{-2} in V, 25.3 in R and 24.2 in I. The 2006 September WFI observations consisted of two pointings that filled in the gap from the missing WFI detector and extended the imaged region. The observing conditions were poor during this run with the seeing in the final combined images being ∼2.8 arcsec. The average 3σ surface brightness limit of this later imaging was 24.1 mag arcsec^{-2} in V, 23.8 in R and 22.7 in I. The extent of the WFI imaging from both runs is shown in Fig. 1. The total imaged area was ∼51 × ∼59 arcmin.

Targets were selected from the WFI imaging for optical spectroscopic followup. Initial target selection was done on the I-band images with confirmation of the targets in the R and V bands. There were many spurious object detections around bright stars, diffraction spikes and chip defects. To remove these, a series of rectangular and circular exclusion regions was defined around the problem areas as seen in Fig. 1.

Objects brighter than a V-band total magnitude of 19.2 were removed from the list of targets for spectroscopic followup. This limit is 0.6 mag fainter than the cD galaxies in Abell 370, and no other cluster members are expected to be this luminous (note: the two cD galaxies were included for spectroscopic followup as additional targets). Objects brighter than V-band total magnitude of 21.7 were used for target selection. A small number of objects were removed from the target list that were substantially redder than galaxies belonging to the red sequence of Abell 370, and hence likely to be stars or distant background galaxies.

Aperture magnitudes were measured using 3 arcsec diameter apertures. Total magnitudes were measured using the best magnitude parameter of SExtractor. All magnitudes were calibrated on the Vega system. Comparisons between the total and aperture magnitudes were used to remove stars from the galaxy sample. The optical magnitudes of the galaxies were corrected for the foreground extinction from the Galaxy using the Schlegel–Finkbeiner–Davis Galactic reddening map (Schlegel, Finkbeiner & Davis 1998). No correction was done for the internal extinction of the galaxies, and it is assumed that any correction would have minimal effect on our results. Separate lists of targets were made from each set of the WFI imaging. Only after applying all the above selection criteria were the target catalogues merged. The photometry is consistent for objects that appear in both catalogues.

2.2 The optical spectroscopic data

Over four nights from 2006 October 11 to 14, the targets were observed with AAOmega, the fibre-fed, dual-beam spectrograph on the Anglo-Australian Telescope (AAT). 11 fibre configurations were observed for 2 hours each. Optical spectra were obtained for a total of 2347 unique targets. The combination of the blue and red arms of the spectrograph provided continuous wavelength coverage from ∼3700 to ∼8800 Å. At the redshift of the cluster ($z = 0.37$), this covers the rest-frame wavelength region from ∼2700 to ∼6400 Å which includes the emission lines of [O II]λ3727, Hβ, [O III]λ4959 and [O III]λ5007 (but not Hα) as well as the absorption features Ca H&K, Na, Mg, Hδ, G band and Hγ.

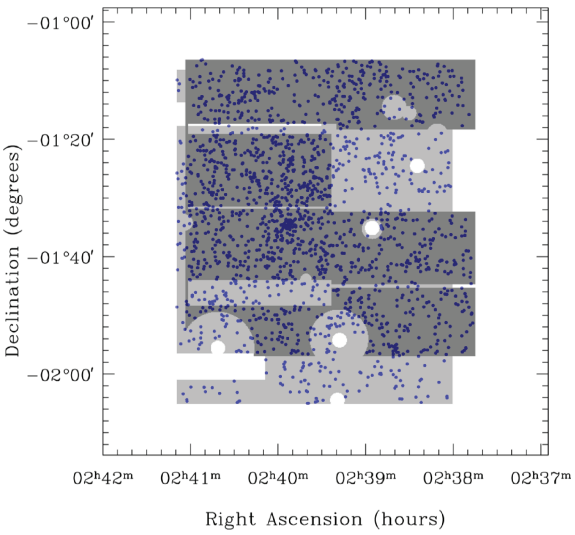

Figure 1. This figure shows the extent of the optical imaging taken with the ANU 40-inch telescope. The dark grey areas were observed in 2005 November; the light grey areas are the additional areas covered in 2006 September. The circles are the regions around bright stars where galaxy identification could not be made. The circles are larger in the 2005 November observations as the better seeing caused the brightest stars to saturate the CCD. The small points are the 1877 objects for which redshifts were obtained during the AAOmega run in 2006 October.

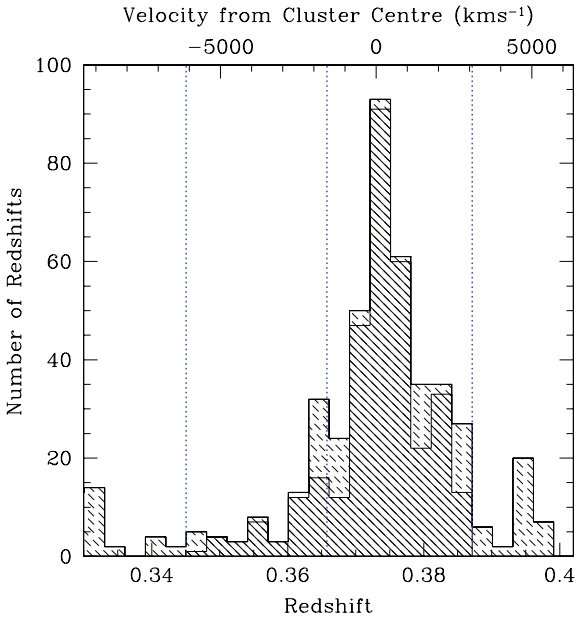

Figure 2. This figure shows the distribution of the 450 redshifts around the galaxy cluster Abell 370. The vertical dotted lines are the GMRT frequency limits converted to their H I redshift; the central dotted line is the boundary between the upper and lower sidebands of the GMRT radio data. The histogram shaded with the unbroken line is the distribution of the 324 redshifts used in H I co-adding. The histogram shaded with the broken line is the distribution of the unusable redshifts (see Section 4 for details). The top x-axis shows the velocity from the cluster centre, giving an indication of the peculiar motion of the galaxies within the cluster. The cluster centre is at $z_{cl} = 0.373$ and the listed velocity includes the cosmological correction (i.e. it is divided by $1 + z_{cl}$).

The data were reduced using the Anglo-Australian Observatory's 2DFDR data reduction pipeline[1] and the redshift determination was done with the interactive software package RUNZ. In total there were 1877 objects with secure redshifts (includes both galaxies and some foreground stars), a redshift completeness of 80 per cent. The objects range in redshift from $z \sim 0$ to 1.2, and the error in the redshifts is $\sim$70 km s^{-1}. There are 450 galaxies with redshifts between $z = 0.33$ and 0.40 (see Fig. 2 for the redshift distribution); 324 of these galaxies were usable for H I co-adding (see Section 4 for details on this selection).

2.3 The optical properties of the Abell 370 galaxies

Fig. 3 shows the 324 galaxies used in the H I co-adding plotted as projected distance in Mpc from the galaxy cluster centre. Plotted in this figure is the extent of the hot intracluster gas, the X-ray significance radius. This is the radius from the cluster centre where the X-ray emission surface brightness has fallen to three times the background sky level (the 3σ extent of the X-ray gas). For the cluster Abell 370, this radius is at 1.45 Mpc (4.7 arcmin) (Ota & Mitsuda 2004). Also plotted in this figure is the R_{200} radius, the radius at which the cluster is 200 times denser than the general field (Carlberg et al. 1997). For Abell 370, this is $R_{200} = 2.57$ Mpc which was derived from the cluster velocity dispersion of 1263 km s^{-1}. The cluster velocity dispersion of Abell 370 was measured from the redshifts obtained in this work (Pracy et al., in preparation).

[1] Anglo-Australian Observatory web site http://www.aao.gov.au/AAO/2df/aaomega/aaomega.html.

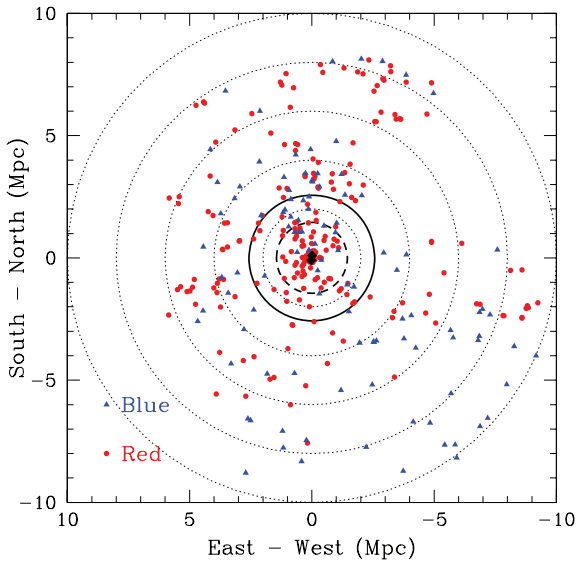

Figure 3. This figure shows the 324 galaxies used in the H I co-adding plotted as projected distance in Mpc from the galaxy cluster centre. The triangular points are the blue galaxies and the circular points are the red galaxies. The two diamond points near the centre are the two cD galaxies. The dashed circle is the 3σ extent of the X-ray gas (Ota & Mitsuda 2004) and is at a radius of 1.45 Mpc. The solid circle is the R_{200} radius of 2.57 Mpc. The faint, dotted circles are at radii of 2, 4, 6, 8 and 10 Mpc from the cluster centre.

For galaxies near the redshift of the cluster at $z = 0.37$, inter-band K-corrections were performed using the methodology of Kim, Goobar & Perlmutter (1996) and Schmidt et al. (1998). The observed R-band magnitudes were K-corrected to rest-frame B-band and the observed I-band magnitudes to rest-frame V band. Input spectra were created using linear combinations of pairs of galaxy template spectra that reproduce the observed galaxy $V - I$ colour within the photometric uncertainties. The final K-correction value is derived from the mean of the corrections derived from these input spectra.

The $B - V$ colour versus B-band magnitude diagram for all the 324 galaxies used in the H I co-adding can be seen in the left-hand panel of Fig. 4 and for those galaxies within 1.45 Mpc of the galaxy cluster centre (the X-ray significance radius) in the right-hand panel. A least absolute deviation regression fit was made to the cluster ridgeline in the colour–magnitude diagram containing those galaxies within 1.45 Mpc of the cluster centre. The slope of this linear fit was close to zero, so a fixed colour term for the ridgeline of $B - V = 0.77$ was used. This almost zero slope is probably due to the limited magnitude range used and the large errors in the optical magnitudes ($\sim$0.1 mag). The galaxies were divided into blue and red galaxies using the Butcher–Oemler condition, i.e. the blue galaxies are those at least 0.2 mag bluer than the cluster ridgeline (Butcher & Oemler 1984). This sets the division at $B - V = 0.57$. In Fig. 3, which shows the projected distance distribution of the galaxies, the blue and red galaxies are plotted using different symbols. Near the cluster core the red galaxies dominate. Away from the cluster centre the number of blue galaxies increases, though a large number of these outer galaxies are red. The blue fraction of galaxies in the cluster using the Butcher–Oemler criteria is 0.132 ± 0.003 within the measured R_{30} radius of 0.669 Mpc (2.17 arcmin). (R_{30} is defined as the radius containing 30 per cent of the projected galaxies that lie within 3 Mpc of the cluster centre.) The blue fraction found in

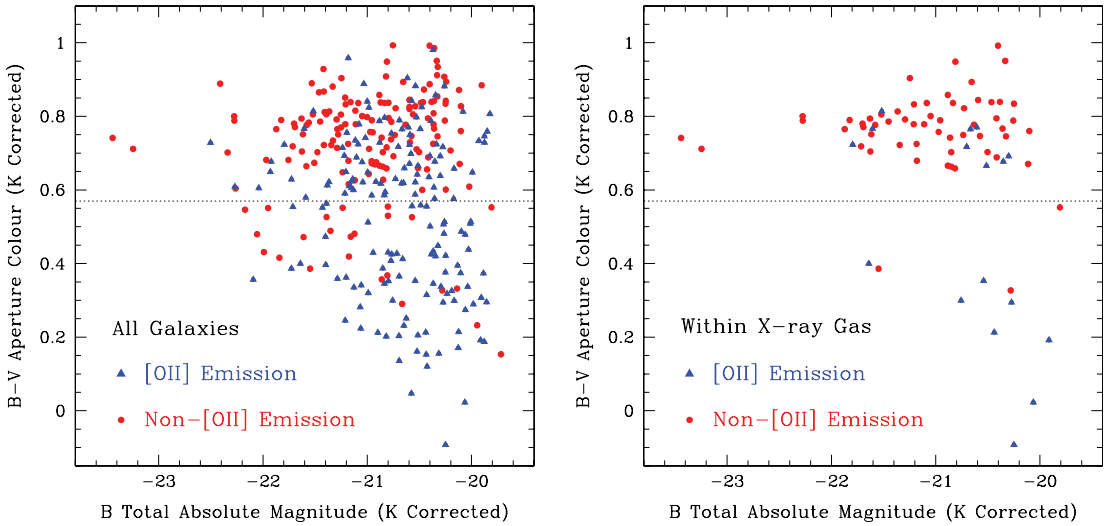

Figure 4. In the left-hand panel is the $B - V$ aperture colour versus B-band total absolute magnitude for the 324 galaxies used in the H I co-adding. The right-hand panel shows the same for the 75 galaxies close to the galaxy cluster centre (within a projected distance from the cluster centre of 1.45 Mpc, the 3σ extent of the X-ray gas). The triangular points are galaxies with measured [O II] equivalent widths >5 Å, and the circular points are those with [O II] equivalent widths ≤5 Å. The dotted line is the dividing line used to separate the blue and red galaxies at $B - V = 0.57$.

the majority of nearby clusters is ∼0.03 (Butcher & Oemler 1984), substantially lower than that found in Abell 370.

The equivalent width of the [O II]λ3727 emission line was measured from the AAOmega optical spectra using the standard flux-summing technique. The galaxies were divided into [O II] emission and non-[O II] emission samples at an equivalent width of 5 Å. This is roughly the 2σ limit for the equivalent width measurements. It was not possible to identify the active galactic nuclei (AGN) in this sample as the optical spectra at $z = 0.37$ did not include the Hα and [N II] lines, which are required for the standard AGN diagnostic test (Baldwin, Phillips & Terlevich 1981). In the colour–magnitude diagrams of Fig. 4, the [O II] emission and non-[O II] emission galaxies are plotted using different symbols. Around the cluster centre (the right-hand panel of Fig. 4), there are few [O II] emission galaxies. For all 324 galaxies (the left-hand panel of Fig. 4), the majority of the blue galaxies have [O II] emission but the red galaxies are almost evenly split between emission and non-emission galaxies. The $B - V$ colour versus [O II] equivalent width for all the 324 galaxies used in the H I co-adding can be seen in Fig. 5. A trend is seen with bluer galaxies having a larger [O II] equivalent width. However, there is a large amount of scatter in this relationship which is mostly due to real astrophysics variation, i.e. not due to random statistical errors.

The SFR for the galaxies at redshifts near Abell 370 was calculated from the [O II]λ3727 emission line. The [O II] line flux for the galaxies was estimated using the measured equivalent width from the optical spectra and the broad-band photometry from the optical imaging. A correction for internal dust extinction in the galaxies was made to the [O II] line flux by assuming the canonical 1 mag extinction at Hα (Kennicutt 1983; Niklas, Klein & Wielebinski 1997). This was converted to an extinction at the wavelength of [O II]λ3727 using the extinction relation of Calzetti (1997). This correction increases the [O II] flux by a factor of 5.15. The [O II] line luminosity was converted to an SFR using equation (4) of Kewley, Geller & Jansen (2004). The errors in the derived SFRs are based on a combination of the statistical errors in the spectral line fits, the intrinsic error in the conversion from [O II] luminosity to SFR and the scatter in the internal dust extinction correction which is

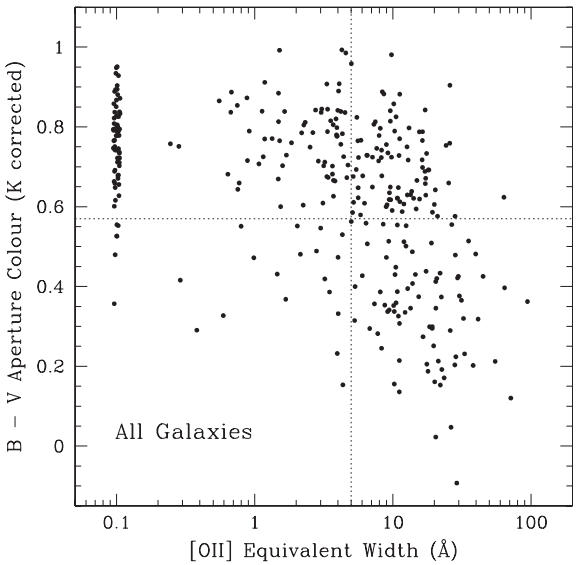

Figure 5. This figure shows the $B - V$ aperture colour versus [O II] equivalent width for all the 324 galaxies used in the H I co-adding. The 68 galaxies that have measured [O II] equivalent widths equal to or less than zero have been given a value of ∼0.1 Å so that they can be plotted on the log scale used here. The dashed vertical line is the [O II] cut used to separate emission from non-emission galaxies (at 5 Å) and the horizontal line is the colour cut used to separate blue and red galaxies (at 0.57 mag).

of the order of 50 per cent (Kennicutt 1983). The dust correction dominates the error and limits the precision for the measured SFR of individual galaxies to a percentage error of at best 55 per cent. However, the average SFR of the galaxies can be derived with significantly higher precision, assuming the error is purely random, i.e. there are no systematic offsets.

For extended detail on the optical data reduction and analysis, see Pracy et al. (in preparation).

2.4 The comparison of the properties of galaxy subsamples

In this work, the Abell 370 galaxies have been broken up into a number of subsamples based on their optical colour, spectroscopic properties and location in the cluster (their galaxy environment). The galaxies are divided into optically blue and red galaxy subsamples at $B - V = 0.57$, as discussed previously. Out of the 324 galaxies used in the H I co-adding, there are 219 red and 105 blue galaxies. The galaxies are divided into [O II] emission and [O II] non-emission galaxy subsamples at [O II] equivalent width of 5 Å, as discussed previously. Out of the 324 galaxies used in the H I co-adding, there are 156 non-[O II] emission galaxies and 168 [O II] emission galaxies. An inner subsample of galaxies was selected that lie within a projected distance of 2.57 Mpc (the R_{200} radius) of the cluster centre. To remove a handful of galaxies that were clearly foreground to the cluster, galaxies in this subsample were also required to lie within four times the velocity dispersion of 1263 km s^{-1} of the cluster centre ($z_{\rm cl} = 0.373$), a redshift range of $z = 0.356$–0.390. Using these criteria, there are 110 galaxies in the inner subsample, leaving 214 galaxies in an outer subsample, away from the cluster centre.

These subsamples will be important in Section 5, where the H I content of each galaxy subsample is considered. Each of the Abell 370 subsamples shares a number of galaxies in common. Understanding the overlap between the subsamples is critical for interpreting the different H I measurements made. The distribution of various properties for each of the subsamples is shown in Fig. 6.

The top panels of Fig. 6 show distribution of the B-band total absolute magnitude of the galaxies broken up into colour, emission type and cluster location in the left-hand, middle and right-hand panels, respectively. The blue galaxies, on average, tend to be slightly fainter than the red galaxies. The [O II] and non-[O II] emission galaxies span similar ranges in absolute magnitude as do the outer and inner subsamples. In this comparison, we are ignoring the two red cD galaxies that are both brighter than -23 B-band total absolute magnitude.

The middle panels of Fig. 6 show the distribution of the $B - V$ colour for the galaxies broken into the different subsamples. In panel (d), which breaks the galaxies into blue and red colours, the $B - V$ colour shows only that there are considerably more red galaxies than blue galaxies. Panel (e), which displays the emission subsamples, shows that the [O II] emission galaxies span the complete colour range from blue to red. The non-[O II] emission galaxies are much more tightly grouped, with most being red in colour with only a small tail of blue galaxies. Panel (f) shows the colour distribution of the inner and outer cluster galaxies. Not surprisingly the inner sample is dominated by red galaxies while the outer galaxies have a more even distribution of colours, though there are still more red galaxies than blue galaxies (136 red to 84 blue) in the outer sample.

The bottom panels of Fig. 6 show the distribution of the [O II] equivalent width of the galaxies broken into the different subsamples. Panel (g) shows the [O II] equivalent width distribution for the blue and red galaxies. While the galaxies with the very largest equivalent widths are dominated by the blue galaxies, there is a fair amount of overlap between the red and blue galaxies in the intermediate equivalent width values. Below 5 Å (the cut-off used in the [O II] samples), the galaxies are dominated by the red galaxies with the blue galaxies tailing off. Of the 168 galaxies above the 5 Å cut-off, there are 87 red and 81 blue galaxies; below the cut-off, there are 132 red and only 24 blue galaxies. In panel (h), the [O II] equivalent width is broken up into the [O II] emission and non-[O II] emission samples at the 5 Å value. The most common equivalent width value for galaxies with [O II] emission lies around 15 Å. Panel (i) shows the distribution of the [O II] equivalent width for the outer and inner cluster galaxies. There is a greater fraction of [O II] emission galaxies in the less dense region away from the cluster centre. This agrees with the star formation–density relationship found by Balogh et al. (1998) in clusters from $0.18 < z < 0.55$ using [O II] emission.

3 THE RADIO DATA

Radio observations of the galaxy cluster Abell 370 were carried out in 2003 August 10–17 using the Giant Metrewave Radio Telescope (GMRT) in India. A total of 63 hours of telescope time was used, with 34 hours of on-source integration after the removal of the slewing time, flux and phase calibrator scans. After flagging, ∼63 per cent of the visibilities for the lower sideband and ∼50 per cent of the visibilities for the upper sideband of this on-source data remained (50 per cent of the total GMRT visibilities provide an equivalent sensitivity as an integration with ∼21 of the 30 GMRT antennas working perfectly for the entire time).

The total observing bandwidth of 32 MHz was split into two 16 MHz-wide sidebands covering the frequency range from 1024 to 1056 MHz which is a redshift range $0.345 < z < 0.387$ for H I 21 cm emission. The pointing centre of the GMRT observations was RA $2^{\rm h}39^{\rm m}42\overset{\rm s}{.}0$ Dec. $-01^\circ37'08''$ J2000 (see Fig. 7). This is 3.7 arcmin from the cluster centre. The reason for the offset was to bring the strong radio continuum source 4C −02.13 closer to the centre of the GMRT primary beam and out of the sidelobes of the primary beam. The data have two polarizations and 128 spectral channels per sideband, giving a channel spacing of 0.125 MHz (36.0 km s^{-1}). Primary flux calibration was done using periodic observations of 3C48, which has a flux density at 1040 MHz of 20.18 Jy. Phase calibration was done using scans on the VLA calibrator source 0323+055 for which our observations give a flux density of 3.723 ± 0.061 Jy.

The data reduction was primarily done using AIPS. Each sideband of data was processed separately. Flux and phase calibrations were determined using the bandpass calibration task BPASS, and the solution was interpolated to the data from the calibrator scans. No normalization was done before determining the solutions. The regular phase calibrator scans throughout the observations which allow us to correct for any time variability of the bandpass shape. We have used an imaging pixel size of 0.75 arcsec and an imaging robustness value of 0. The synthesized beam size (resolution) of the data is ∼3.3 arcsec. For primary beam correction, we assumed a Gaussian beam with full width at half-maximum (FWHM) of 32.2 arcmin at 1040 MHz.[2]

When making continuum images, only channels 11–110 (out of the 128 in each sideband) were used. In order to avoid bandwidth smearing, the visibilities were averaged into a new data set consisting of 10 channels, each of which was the average of 10 of the original channels. This new 10 channel $u - v$ data file was made into a single channel continuum image using the AIPS task IMAGR, which combined the channels using a frequency-dependent primary beam correction based on the effective antenna diameter of 37.5 m. This correction assumes that the primary beam is a uniformly illuminated disc of the specified diameter. The value of this diameter was estimated using the known GMRT primary beam size.

[2] National Centre for Radio Astrophysics web site http://gmrt.ncra.tifr.res.in/gmrt_hpage/Users/Help/help.html.

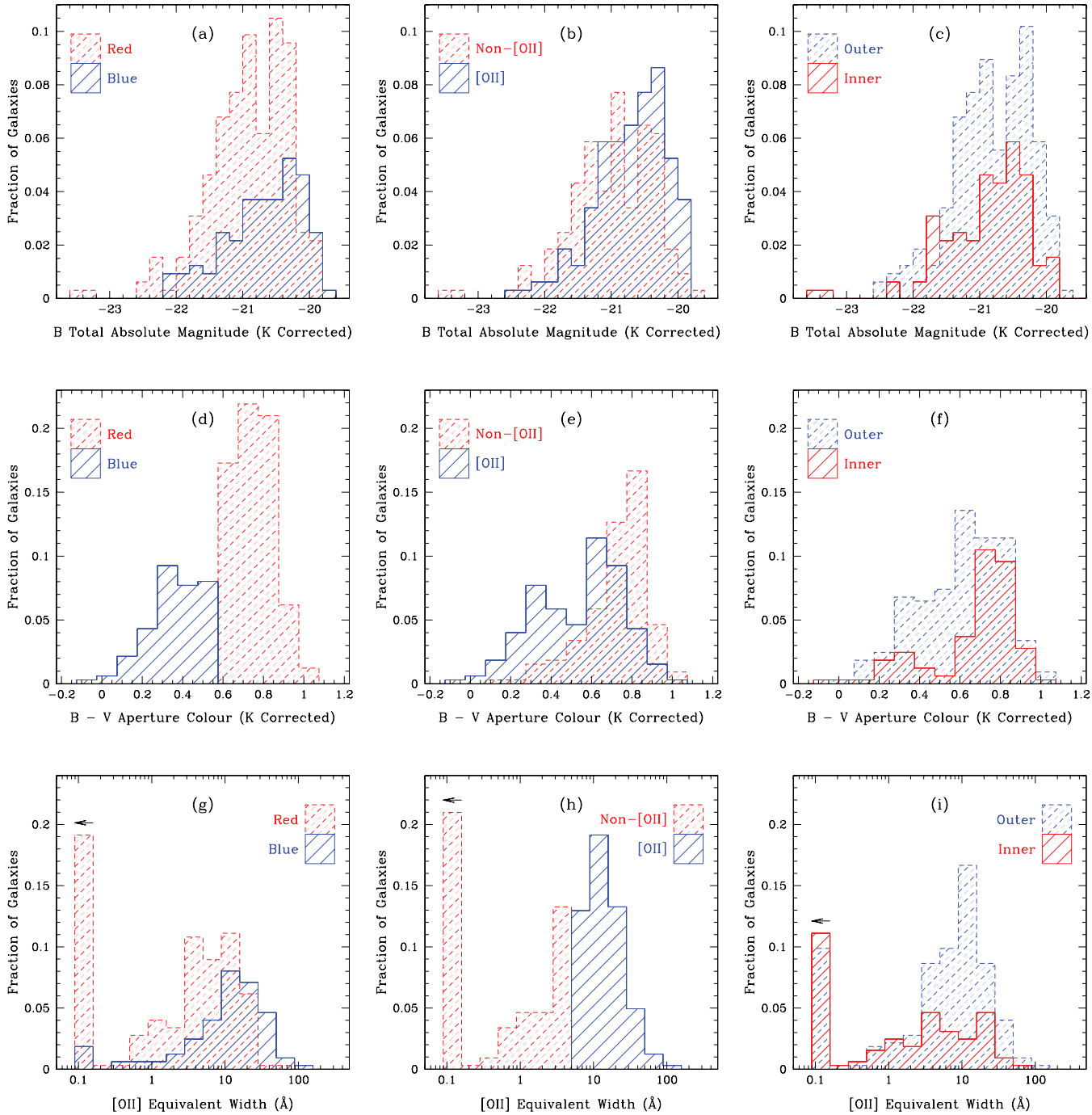

Figure 6. This figure shows the distribution in various parameters of the galaxies within the examined subsamples. The distributions are given as the fraction of the total number of galaxies (324). The parameters considered are the *B*-band total absolute magnitude (top panels), the $B - V$ colour (middle panels) and [O II] equivalent width (bottom panels). The subsamples are the red and blue galaxies (left-hand panels), [O II] and non-[O II] emission galaxies (centre panels) and the inner and outer cluster galaxies (right-hand panels). In the bottom panels, galaxies with [O II] equivalent widths that are zero or negative have been given a value of 0.1 Å to allow them to be plotted on the log scale used. In the [O II] equivalent width histograms, these galaxies are in the last bin which is marked with an arrow on top.

Self-calibration of the data was done using the six brightest radio continuum sources in the field. These sources have raw flux density values (not corrected for the primary beam shape) ranging from 18 to 80 mJy. The self-calibration of GMRT data sometimes does not converge quickly, probably as a consequence of the GMRT hybrid configuration. Radio continuum sources that lack coherence in the synthesis image due to phase errors tend to remain defocused during self-calibration. To fix this problem, slightly extended sources were replaced in the first self-calibration loop with point sources with the same centroid and flux density as the original source. Further self-calibration loops were done using the clean components in the traditional manner. The observational data for each day were initially self-calibrated alone using four loops of self-calibration (two loops of phase calibration and two amplitude and phase calibration

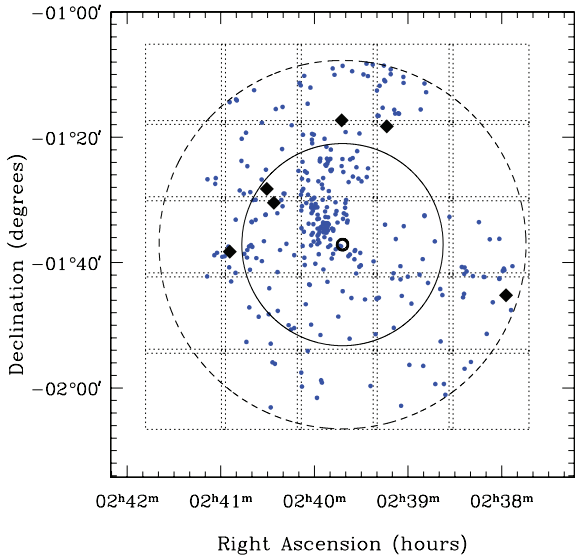

Figure 7. This figure shows the pointing and primary beam size of the GMRT observations with the 324 optical galaxies used in the H I co-adding (the small points). The large diamond points are the radio continuum sources on which self-calibration was performed. The small, bold circle is the centre of the GMRT pointing. The unbroken circle is the primary beam FWHM diameter of 32.2 arcmin and the dashed circle is the 10 per cent primary beam level with diameter of 58.8 arcmin. The dotted, overlapping, square grid shows the 25 facets used to tile the sky in the radio imaging. The centre of this grid pattern was created slightly offset from the GMRT pointing to ensure that all of the 10 per cent level of the primary beam lie within the tiled region.

loops). At this point, the six brightest continuum sources were subtracted from the $u - v$ data, and the data were flagged to exclude any visibility residuals that exceeded a threshold set by the system noise statistics. The continuum sources were then added back into that day's data.

After this detailed editing process, all the $u - v$ data were combined and self-calibration was repeated on the entire combined data set to ensure consistency between the observations on the different days. A large continuum image of the entire field was then made. The AIPS imaging routine assumes that the sky is flat (it ignores the vertical 'w' term). This is an appropriate assumption only for small fields. In order to reduce the distortion over our large field, it was necessary to break the image up into 25 facets (see Fig. 7). Each of these square facets was 12.8 arcmin on a side (1024 pixels) and each overlapped by 38.4 arcsec. The total combined field size was 61.4 arcmin on each side. These overlapping facets cover the region within the 10 per cent primary beam level (58.8 arcmin in diameter). Clean boxes were put around all the discernible continuum sources during the imaging process.

In this initial continuum image, faint sidelobes from the brighter radio sources remained visible which took the form of narrow strips running north–south from the continuum sources. These are residuals from the dirty synthesized beam for the equatorial field that have not been fully removed in the cleaning process. In order to improve the quality of the image, a process of peeling was used to remove the bright sources and these artefacts from the data. This involved removing all continuum sources from the $u - v$ data except for one of the bright sources. A full round of self-calibration was then performed on this new set of $u - v$ data on the single bright source alone. The new calibration derived from the self-calibration (its AIPS SN table) was then applied to the original $u - v$ data (the data with all the continuum sources still in it). The new model of the bright source was then subtracted from this $u - v$ data. Finally, the effect of the new calibration was removed from the $u - v$ data to restore it to its previous calibration by applying the inverse SN table created using the AIPS task CLINV. This process was done for each of the six brightest sources in turn, working from east to west across the field, removing the sources from the $u - v$ data.

The final continuum image was made from this new $u - v$ data set. This image has an rms of 20 μJy. The astrometry of the radio continuum sources in the data was checked against their positions in the VLA Faint Images of the Radio Sky at Twenty-Centimeters (FIRST) survey (Becker, White & Helfand 1995). They show good astrometric agreement of -0.27 ± 0.11 arcsec in RA and 0.24 ± 0.31 arcsec in Dec. Several objects showed good alignment between their optical and radio continuum components suggesting that the optical and radio astrometry is in good agreement.

The remaining radio continuum sources were subtracted from the $u - v$ data using the AIPS task UVSUB. The final spectral data cube was made from this $u - v$ data set. While UVSUB removed most of the continuum emission, some small residuals remained. To remove these final traces, a linear fit to the continuum across frequency was subtracted in the final data cube using the AIPS task IMLIN. This introduces a small bias to the data cube, since any line emission from the galaxies would be included in the fit. The correction for this bias is described in Section 4. In the final data cubes, the median rms was 152 μJy per channel in the lower sideband and 174 μJy per channel in the upper sideband.

4 MEASURING THE H I 21 CM EMISSION SIGNAL FROM THE ABELL 370 GALAXIES

Directly detecting the H I 21 cm emission from even the most gas-rich galaxy in the observed radio data for Abell 370 is unlikely. For a galaxy to be directly detected at 5σ significance, it would need to have an H I mass of at least $M_{\rm HI} = \sim 5 \times 10^{10}\,{\rm M}_{\odot}$, have a velocity width of 300 km s^{-1} and the signal to be all contained within a diameter of ∼3.3 arcsec (17 kpc at $z = 0.37$). In the volume probed by our observations, it is unlikely to find a galaxy with such a large H I mass. Additionally, the H I gas in such a galaxy would likely extend out to a much greater diameter, making it even harder to detect in our data. A search of the radio data cube for H I direct detections was made using the DUCHAMP software developed by Matthew Whiting of the Australia Telescope National Facility. Nothing of significance was found as expected.

Instead of direct detection, the H I 21 cm emission signal from multiple galaxies has been co-added to increase the signal-to-noise ratio of the measurement. This stacked signal can then be used to quantify the total H I gas content of the galaxies. The galaxies are located in the radio data using their measured optical positions and redshifts.

The expected frequency of the H I 21 cm emission from each galaxy is determined from their optical redshift. Of the 1877 optical redshifts obtained, 324 are usable for H I co-adding. The optical redshift distribution for galaxies around the cluster at $z = 0.37$ can be seen in Fig. 2. Only redshifts that lie within the H I frequency range covered by the radio data of $z = 0.3451$–0.3871 could be used in the co-adding. The galaxies used for co-adding were also limited to those inside the 10 per cent GMRT primary beam level. Redshifts that lie within seven channels (0.875 MHz) of the boundary between the two radio sidebands (this is $z \sim 0.3658$) were also excluded. Finally, redshifts that lie in the nine channels (1.125 MHz)

surrounding some strong radio interference in the lower sideband were excluded from the co-adding. This strong radio interference is located at ∼1030 MHz (H I redshift $z = 0.379$).

The H I 21 cm emission signal of a galaxy is spread over a velocity width (frequency width) determined by the motion of the H I gas within the galaxy. If the gas in the galaxy is rotating in a disc, then the inclination of the disc to the observer will have a substantial effect on the observed velocity width. A rotating disc galaxy will have its largest velocity width when its disc is viewed edge on by an observer and its smallest velocity width when its disc is viewed face-on. Assuming minimal H I self-absorption, galaxies with the same H I mass but different disc inclinations should have the same integrated H I flux. However, the peak H I flux of these galaxies will vary greatly depending on their disc inclinations. The peak flux will be a maximum when its disc is face-on, i.e. when the velocity width is at a minimum.

Assuming a random distribution of disc orientations, 50 per cent of disc galaxies will have inclinations to the observer of greater than 60° (edge on) and only 13 per cent galaxies will have inclinations less than 30° (face-on). By selecting the galaxies in the optical, a higher proportion of the disc galaxies in our sample will be edge on compared to H I selected samples. This is due to a combination of this preferred orientation and because edge-on galaxies have higher optical surface brightnesses making them easier to detect than face-on systems. As a result of this selection effect, the galaxies in our sample with the most H I gas (the spiral disc galaxies) are likely to have large H I velocity widths. Unfortunately, it is not possible to measure the inclination of the disc galaxies in our sample due to the combination of the poor seeing in our optical imaging and the small angular size of the galaxies at redshift of $z = 0.37$.

As we do not detect the individual H I 21 cm emission of the galaxies, we cannot measure their individual galaxy velocity widths. Instead we have to make some reasonable assumptions and define a velocity width that should encompass all the co-added H I 21 cm emission signal from the galaxies. From the H I Parkes All Sky Survey (HIPASS) (Meyer et al. 2004), a galaxy with $M_{\rm H\,I} = \sim 10^9\,{\rm M}_\odot$ has a maximum velocity width of ∼250 km s^{-1} and a galaxy with $M_{\rm H\,I} = \sim 10^{10}\,{\rm M}_\odot$ has a maximum velocity width of ∼400 km s^{-1} (w_{50}). Galaxies with low disc inclinations can have markedly narrower velocity widths than these maxima. Using the optical Tully–Fisher relationship from McGaugh et al. (2000) and assuming no inclination correction, the median-estimated velocity width (w_{20}) based on the *B*-band absolute magnitudes of the Abell 370 galaxies is ∼320 km s^{-1}.

The statistical uncertainty in the optical redshifts obtained for Abell 370 is ∼70 km s^{-1}. When co-adding the galaxies, this redshift uncertainty will broaden the resulting H I emission signal. This redshift broadening is taken into account by increasing the H I velocity width used by $\pm 2\sigma$ (280 km s^{-1}). To ensure that all the H I signals from all the combined galaxies are measured, a velocity width of 600 km s^{-1} was used. This velocity width takes into account the width of the larger galaxies in the sample as well as the effect of the redshift broadening. The uncertainty due to noise in the measured co-added H I 21 cm emission signal is approximately proportional to the square root of the velocity width used. A narrower velocity width will have a smaller estimated error but will likely miss some of the H I signal.

When making the final data cube, a linear fit to the spectrum through each sky pixel was subtracted to remove the residuals left from the continuum sources (see the discussion on IMLIN in Section 3). Any H I signal would be included in the calculation of this linear fit across frequency, and this would create an overestimation in the continuum fit, creating a bias in the final H I spectrum. To remove this bias, the H I spectrum for each galaxy has a new linear fit made across all frequency channels except those corresponding to a 600 km s^{-1} velocity width around the galaxy at its redshift (these should be the channels that would contain any H I signal). This fit is then subtracted from the data, removing any bias created by IMLIN. This correction increases the H I flux density measured in the co-added spectra of different subsamples of galaxies from anywhere from 20 to 40 per cent.

Variance weighting is used when co-adding the separate H I spectra. The variance is calculated from the known rms per frequency channel in the radio data cube, factoring in the primary beam correction for galaxies away from the beam centre. Variance weighting provides the optimal signal-to-noise ratio for the co-added H I signal. However, it does introduce a potential bias as those galaxies located near the cluster centre are given higher weight as they are close to the GMRT pointing centre. The measured H I 21 cm emission flux density can be converted to the mass of atomic hydrogen that produced the signal by the following relation:

$$M_{\rm H\,I} = \frac{236}{(1+z)} \left(\frac{S_{\rm v}}{\rm mJy}\right) \left(\frac{d_{\rm L}}{\rm Mpc}\right)^2 \left(\frac{\Delta V}{\rm km\,s^{-1}}\right), \quad (1)$$

where $S_{\rm v}$ is the H I emission flux density averaged across the velocity width ΔV and $d_{\rm L}$ is the luminosity distance to the source. This equation assumes that the cloud of atomic hydrogen gas has a spin temperature well above the cosmic background temperature, that collisional excitation is the dominant process and that the cloud is optically thin (Wieringa, de Bruyn & Katgert 1992). No correction for H I self-absorption has been made to any of the measurements. H I self-absorption may cause an underestimation of the H I flux by as much as 15 per cent. However, this value is extremely uncertain (Zwaan et al. 1997). In this analysis, the galaxies were all assumed to be at the distance of the cluster centre at $z_{\rm cl} = 0.373$, a luminosity distance of $d_{\rm L} = 2000$ Mpc.

It is not possible to measure the projected extent of the H I gas on the sky for the galaxies, as we do not detect their individual H I 21 cm emission. The calibrator convention for synthesis images means that the peak specific intensity of an unresolved source is equal to the total flux density of that source. This means that, if a galaxy is unresolved by the GMRT synthesized beam, we can take the value of the specific intensity at the optical position of the galaxy as a measure of the total H I flux density of the galaxy. The GMRT synthesized beam has an FWHM ∼3.3 arcsec at 1040 MHz which corresponds to ∼17 kpc at $z = 0.37$. Unfortunately, all but the very smallest of the galaxies in our sample are likely to be resolved by this synthesized beam size. The solution to this problem is to smooth the radio data to larger synthesized beam sizes until the galaxies are unresolved and then measure their H I signal.

The Gaussian smoothing in the image plane is equivalent to tapering (multiplying by a Gaussian) in the u–v plane. This effectively reduces the weight of the longer GMRT baselines in the image plane. Thus smoothing to larger synthesized beam sizes increases the rms noise in the radio data. However, the measured H I flux density increases for galaxies that are now unresolved in the new smoothed data. From the initial radio data with synthesized beam size ∼3.3 arcsec (∼17 kpc at $z = 0.373$), smoothed data sets were created with circular synthesized beam sizes in 10 kpc steps, i.e. equal to 30, 40, 50, 60, 70, 80, 90 and 100 kpc (5.8, 7.8, 9.7, 11.7, 13.6, 15.5, 17.5 and 19.4 arcsec). The smoothing was done with the AIPS task SMOTH. The rms per channel in the radio data increases from ∼160 μJy at a synthesized beam size of 17 kpc (∼3.3 arcsec),

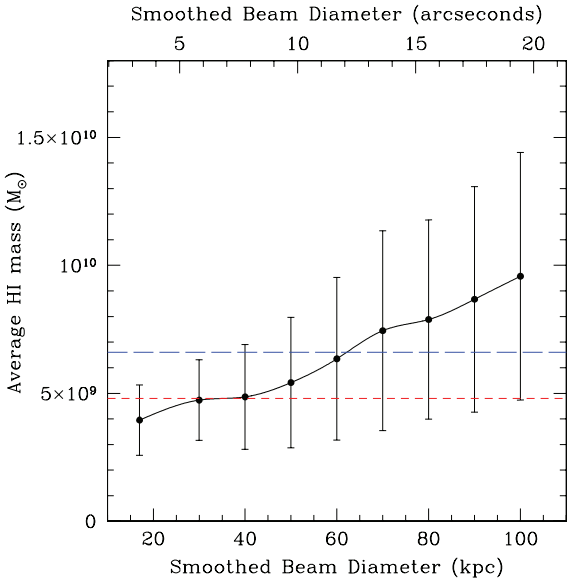

Figure 8. This figure shows the average H I mass for all 324 Abell 370 galaxies measured in the different smoothed synthesized beam size data. The short dashed line shows the H I mass for the mid-smoothing measurement and the long dashed line shows the H I mass for the large smoothing measurement (see text for details).

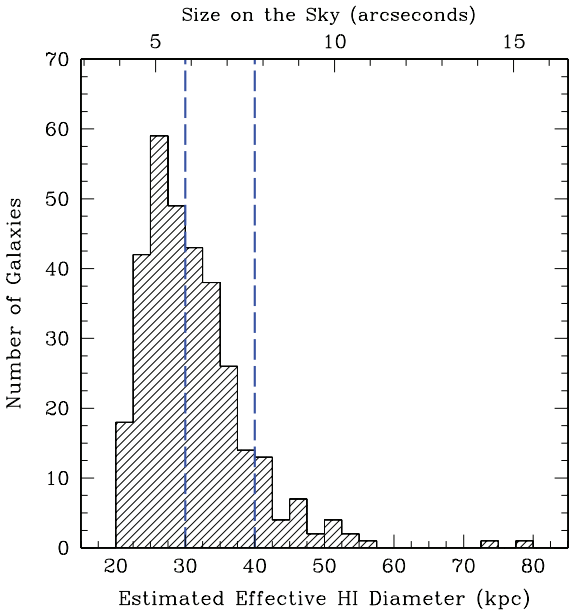

Figure 9. This figure shows the estimated H I effective diameter (the diameter within which half the H I mass is contained) for the 324 galaxies that are used in the H I co-adding. The diameter was derived from the relationship between H I size and optical magnitude found for spiral and irregular galaxies in the field (Broeils & Rhee 1997). The dashed lines mark the values used to split the galaxies into the small, medium and large categories. The top *x*-axis displays the size the galaxies would appear on the sky at the redshift of the cluster ($z_{\rm cl} = 0.373$).

to ∼280 μJy at 50 kpc (9.7 arcsec) and to ∼550 μJy at 100 kpc (19.4 arcsec).

The co-added H I 21 cm flux density for all 324 galaxies in the sample was measured in each set of smoothed data and converted to the equivalent average H I mass as seen in Fig. 8. In this figure, the measured H I mass can be seen to rise with increasing synthesized beam size. This indicates that the H I gas extends beyond the inner regions of the galaxies that is probed by the smaller synthesized beam sizes. As the synthesized beam size increases, the error also increases making it difficult to precisely define the extent of the H I signal.

An estimate of the projected size of the H I gas in a galaxy can be used to determine the minimum synthesized beam size that would leave the galaxy unresolved. This enables a definite measurement of the total H I gas as well as reducing the error introduced by smoothing the data. An estimate of the H I size of a galaxy can be made using the correlation found between the optical *B*-band magnitude and H I size of spiral and irregular galaxies in the field at low redshift (Broeils & Rhee 1997). This relationship is

$$\log(D_{\rm eff}) = -(0.1588 \pm 0.011)B_{\rm abs} - (1.827 \pm 0.22), \quad (2)$$

where $D_{\rm eff}$ is the diameter within which half the H I mass of the galaxy is contained and is measured in kpc. Fig. 9 shows the distribution of the estimated effective H I diameter for the 324 galaxies around Abell 370. The galaxies are broken up into three groups based on their estimated $D_{\rm eff}$. Small galaxies are defined as those with $D_{\rm eff} \leq 30$ kpc, medium galaxies as those with $30 < D_{\rm eff} \leq 40$ kpc and large galaxies as those with $D_{\rm eff} > 40$ kpc. The 30 kpc value corresponds to an absolute *B*-band magnitude of −20.8 and the 40 kpc value to −21.6. There are 168 small galaxies, 121 medium-sized galaxies and 35 large galaxies in the sample.

Galaxies that have $2 \times D_{\rm eff}$ = synthesized beam size have peak specific intensity values that are ∼90 per cent of their total flux density (assuming a Gaussian shape to the H I gas spatial distribution). In previous co-adding H I work looking at star-forming field galaxies at $z = 0.24$ (Lah et al. 2007), this was the criterion used with the estimated $D_{\rm eff}$ to determine the maximum synthesized beam size in which a galaxy would be unresolved. However, the relationship found by Broeils & Rhee (1997) was for spiral and irregular galaxies in the field, while the galaxies in Abell 370 are a mixture of early- and late-type galaxies in a variety of environments. This criterion will likely overestimate the true extent of the H I gas for many of the galaxies.

Three different measurements of the average H I gas mass are made to reflect this uncertainty in the H I extent of the galaxies. The first co-added H I mass measurement is made by measuring the specific intensity at the optical positions of the galaxy in the original unsmoothed GMRT radio data (synthesized beam size of 17 kpc, ∼3.3 arcsec). For all 324 galaxies, the measured average H I mass in this unsmoothed measurement is $(4.0 \pm 1.4) \times 10^9\,{\rm M}_\odot$. The second co-added H I mass measurement is made by first breaking the galaxies into their small, medium and large size groups based on their estimated $D_{\rm eff}$. The H I flux density for each group of galaxies is then measured in the radio data that has $D_{\rm eff} \leq$ the smoothed synthesized beam size (30, 40 and 50 kpc beam sizes). The three measured values are then combined to give a single average H I flux density. For all 324 galaxies, the measured average H I mass in this mid-smoothed measurement is $(4.8 \pm 1.8) \times 10^9\,{\rm M}_\odot$. A third measurement is made similarly, except each group of galaxies is measured in the radio data that has $2 \times D_{\rm eff} \leq$ the smoothed synthesized beam size (60, 80 and 100 kpc beams sizes). This large smoothing measurement should give an accurate reflection of the total H I gas mass for the galaxies that have similar H I extents to the field spiral and irregular galaxies observed by Broeils & Rhee (1997). For all 324 galaxies, the measured average H I mass in this large smoothed measurement is $(6.6 \pm 3.5) \times 10^9\,{\rm M}_\odot$.

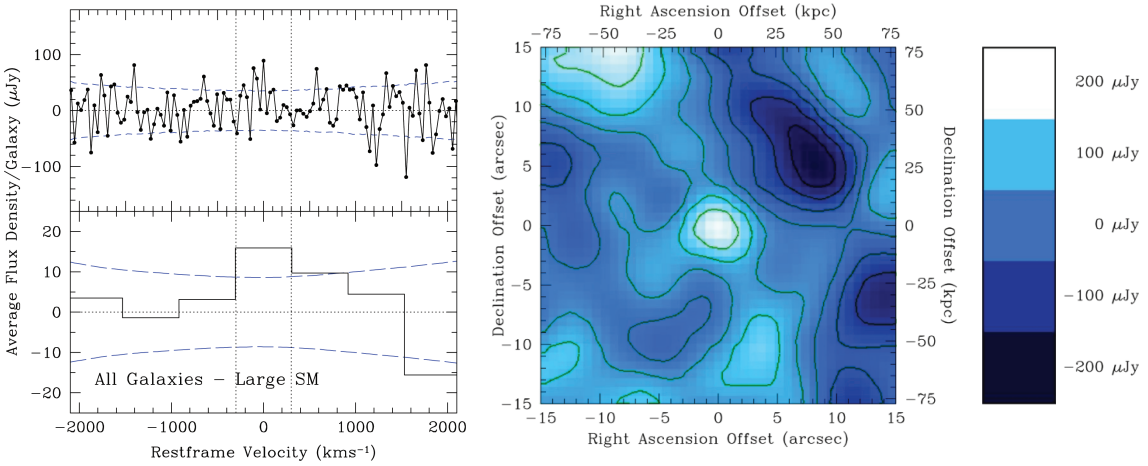

Figure 10. The left-hand panel shows the average H I galaxy spectrum created from co-adding the signal of all 324 galaxies using the large spatial smoothing. The top spectrum has no smoothing or binning and has a velocity step size of 36.0 km s^{-1} . The bottom spectrum has been binned to 600 km s^{-1} . This is the velocity width that the combined H I signal of the galaxies is expected to span. For both spectra, the 1σ error is shown as dashed lines above and below zero. The right-hand panel shows the average H I image made by co-adding the data cube around each of the 324 galaxy and binning across 17 spectral channels (600 km s^{-1}). The radio data used for this image are that smoothed to a synthesized beam size of 5.8 arcsec (30 kpc at $z = 0.373$). The image size is shown in both arcsec and in kpc on opposite axes. The contour levels are −150, −100, −50, 0, 50, 100 and 150 μJy.

The left-hand panel in Fig. 10 shows the weighted average H I spectrum from co-adding the signal from all 324 galaxies using the large smoothing criteria. To estimate the error in the H I measurements, a series of artificial galaxies with random positions and random H I redshifts was used to create co-added random spectra. From many such artificial spectra, a good estimate of the noise level in the measured real H I spectrum could be determined. As seen in Fig. 10, the noise level increases with increasing velocity offset from the centre of the co-added spectrum. This is because some galaxies lie at redshifts (frequencies) near the edges of the radio data cube. When adding the spectra of these galaxies to the total, there are no data for velocities that correspond to frequencies that lie off the edge of the data cube. These velocities with no data are given zero weight in the co-added sum resulting in a higher noise level at these velocities in the final co-added spectrum.

The right-hand panel in Fig. 10 shows the co-added H I image for all galaxies after averaging the frequency channels across the velocity width of 600 km s^{-1}. The radio data used for this image were that smoothed to a synthesized beam size of 30 kpc (5.8 arcsec), i.e. the galaxies have not been broken up into the groups of small, medium and large. As such the signal-to-noise ratio is not the maximum measured.

5 THE H I 21 CM EMISSION SIGNAL FROM SUBSAMPLES OF GALAXIES

The 324 Abell 370 galaxies used in the H I co-adding are a mixture of early- and late-type galaxies in a variety of environments. It is interesting to examine the average H I content of subsamples of galaxies selected by their optical colour, spectroscopic properties or location in the cluster (their galaxy environment). The definition of the major galaxy subsamples considered can be found in Section 2.4, which also details the overlap in their optical properties. The H I mass measurements for various subsamples of the Abell 370 galaxies can be seen in Table 2. The table lists three average H I masses for each subsample; these measurements are the same as used previously for all the galaxies, i.e. unsmoothed, mid-smoothed and large smoothed measurements. These average H I mass measurements are displayed in Fig. 11. From this figure, it can be seen that there are differences not only in the quantity of the H I gas between the subsamples but also in where the H I gas is located within the galaxies.

5.1 The blue and red subsamples

The separation of the Abell 370 galaxies into optically blue and red subsamples was done using the Butcher–Oemler criterion, i.e. the blue galaxies in Abell 370 have $B - V$ colour $\leq$0.57 (see Section 2.3).

In the co-added signal from the 219 red galaxies, the unsmoothed average H I mass measurement is $(2.8 \pm 1.6) \times 10^9\,M_\odot$. Measurements made using the higher smoothing criteria show no increase in the average H I mass and the higher noise in these measurements overwhelms any signal as can be seen in Fig. 11. These results suggest that any substantial quantities of H I gas in the red galaxies must lie within the central regions of the galaxies, i.e. closer than 8.5 kpc to the centre of the galaxies based on the unsmoothed measurement. It is likely that a fair number of these red galaxies have no H I gas. An examination of the data shows that there is no immediately obvious handful of galaxies that have the majority of this H I signal.

In contrast to the red galaxies, co-adding the blue galaxies gives rise to a strong detection of H I 21 cm emission with the observed signal increasing appreciably in the higher smoothing measurements (see Fig. 11). This is similar to the trend seen in H I rich galaxies in the local Universe, which contain large amounts of H I gas that extend beyond their visible stellar discs (Broeils & Rhee 1997). The average H I mass measured for the 105 blue galaxies using the large smoothing criteria is $(19.0 \pm 6.5) \times 10^9\,M_\odot$. The large smoothing criterion, which is based on the H I galaxy sizes of spiral and irregular galaxies in the field, appears to be a good fit to H I gas content of the blue galaxies.

The very different way the H I gas is distributed in the blue and red galaxies can be seen in greater detail in the left-hand panel of Fig. 12. This figure traces the change in H I mass as a function of smoothed

Table 2. This table lists the average galaxy H I mass for subsamples of the Abell 370 galaxies measured using the three different smoothed radio data combinations. The 'H I mass unsmoothed' is the measurement made using only the original GMRT resolution radio data. The 'H I mass mid-smoothing' measurements are made by co-adding different smoothed radio data such that the galaxies have estimated $D_{\rm eff} \leq$ smoothed synthesized beam size and the 'H I mass large smoothing' using $2 \times D_{\rm eff} \leq$ smoothed synthesized beam size. In brackets next to each value is the signal-to-noise ratio of the measurement. $d_{\rm cl}$ is the projected distance in Mpc from the cluster centre and R_{200} is 2.57 Mpc for Abell 370. The two measurements 'within 8 Mpc' subsamples are for comparison with the Coma cluster in Section 6. The selection for these subsamples is more complicated than that listed above (see Fig. 17) (see the text for further details on the subsample selection and smoothing size).

Galaxy sample	Selection criteria	Number of Galaxies	H I mass unsmoothed (10^9 M$_\odot$)	H I mass mid-smoothing (10^9 M$_\odot$)	H I mass large smoothing (10^9 M$_\odot$)
All	–	324	4.0 ± 1.4 (2.9σ)	4.8 ± 1.8 (2.7σ)	6.6 ± 3.5 (1.9σ)
Red	$B - V > 0.57$	219	2.8 ± 1.6 (1.8σ)	2.6 ± 2.1 (1.2σ)	1.4 ± 4.2 (0.3σ)
Blue	$B - V \leq 0.57$	105	7.1 ± 2.7 (2.6σ)	10.0 ± 3.3 (3.0σ)	19.0 ± 6.5 (2.9σ)
Blue, outside X-ray gas	$B - V \leq 0.57$ and $d_{\rm cl} > 1.45$ Mpc	94	8.0 ± 3.2 (2.5σ)	11.1 ± 3.9 (2.8σ)	23.0 ± 7.7 (3.0σ)
Non-[O II] emission	[O II] ≤ 5 Å	156	4.3 ± 1.8 (2.4σ)	5.2 ± 2.4 (2.2σ)	2.3 ± 4.8 (0.5σ)
[O II] emission	[O II] > 5 Å	168	3.6 ± 2.1 (1.7σ)	4.3 ± 2.6 (1.7σ)	11.4 ± 5.2 (2.2σ)
Inner	$d_{\rm cl} \leq R_{200}$ and $z \leq 0.357$	110	3.6 ± 1.7 (2.2σ)	3.9 ± 2.2 (1.8σ)	3.3 ± 4.4 (0.8σ)
Outer	$d_{\rm cl} > R_{200}$ or $z > 0.357$	214	4.6 ± 2.4 (1.9σ)	6.4 ± 3.1 (2.1σ)	12.1 ± 6.1 (2.0σ)
Within 8 Mpc	$d_{\rm cl} \leq 8$ Mpc	220	3.6 ± 1.4 (2.6σ)	4.3 ± 1.9 (2.3σ)	5.1 ± 3.7 (1.4σ)
Blue, within 8 Mpc	$B - V \leq 0.57$ and $d_{\rm cl} \leq 8$ Mpc	58	8.5 ± 3.0 (2.8σ)	11.6 ± 3.7 (3.1σ)	17.5 ± 7.3 (2.4σ)

synthesized beam size for the blue and red galaxies, i.e. not using the galaxy size groupings. The blue galaxies show steady increase in H I gas with smoothing size until it appears to end ~70 kpc. The red galaxies show some H I signal at the lowest smoothing sizes, but the higher beam sizes appear to just add noise obscuring any signal. The co-added H I spectrum for the blue galaxies using the large smoothing criteria can be seen in panel (a) of Fig. 13 and the co-added H I spectrum for the red galaxies using the unsmoothed criteria in panel (d) of this figure.

In the central regions of nearby clusters, late-type galaxies are found to be H I deficient compared to similar galaxies in the field (Haynes et al. 1984). One would like to see if this trend is seen in the late-type galaxies inside the hot intracluster medium of the cluster core of Abell 370 at $z = 0.37$. Assuming that blue galaxies are a representative sample of the late-type galaxies, there are

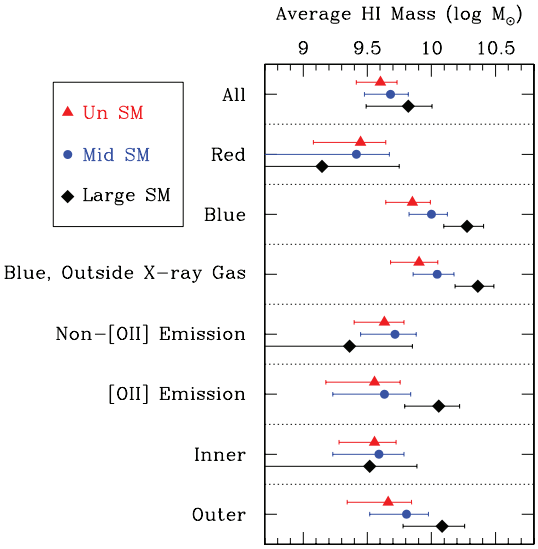

Figure 11. This figure displays the average galaxy H I mass for the different subsamples of galaxies measured using the different smoothed data combinations. The 'Un SM' are the unsmoothed values, 'Mid-SM' the mid-smoothing values and the 'Large SM' are the large smoothing values.

11 such galaxies within the 3σ extent of the X-ray gas (1.45 Mpc from the cluster centre; see Section 2.3). Unfortunately, this is an insufficient number of galaxies to co-added to enable a meaningful measurement of the gas depletion of the galaxies. The best that one can do is consider the subsample of blue galaxies outside the X-ray significance radius of which there are 94. For this subsample, the average H I mass is $(23.0 \pm 7.7) \times 10^9$ M$_\odot$ using the large smoothing criteria. This is larger than that found for the blue subsample as a whole and is the highest significance detection of H I 21 cm emission found in this work. The difference between this subsample and the subsample of all blue galaxies seems to be the greatest in the large smoothing H I measurements; there is only a small increase in the unsmoothed and mid-smoothing values (see Table 2). This suggests that the blue galaxies inside the hot intracluster gas have lost H I gas in their outer regions. This is consistent with how most of the various environment mechanisms would remove the gas in galaxies (see Section 1). This difference in average H I mass for all 105 blue galaxies and the 94 blue galaxies outside the X-ray gas is not statistically significant, but it does follow the expected trend of H I deficiency found in late-type galaxies within nearby clusters.

The left-hand panel in Fig. 14 shows the weighted average H I spectrum from blue galaxies outside the X-ray gas using the large smoothing criteria. The right-hand panel in Fig. 14 shows the co-added H I image for the same galaxies after averaging the frequency channels across the velocity width of 600 km s^{-1}. This image was made using the same method as discussed in Section 4 for the image of all galaxies (seen in Fig. 10) except that data from the larger smoothed synthesized beam of 50 kpc (9.7 arcsec) were used. This was done to highlight the signal from the outskirts of the co-added galaxies which are difficult to see in the smaller beam sized data. The centre of the H I image appears ~2 arcsec different from the centre of the optical galaxies. This is not a real astrometric difference between the radio and optical data. Instead it is an effect of the large smoothed synthesized beam size used and the contribution of a slight positive noise spike (less than 1σ) that is located away from the centre of the image. The good alignment between the optical and radio data can be seen in the images made using the smallest synthesized beam size where only the H I signal from the very central regions of the galaxies is notable.

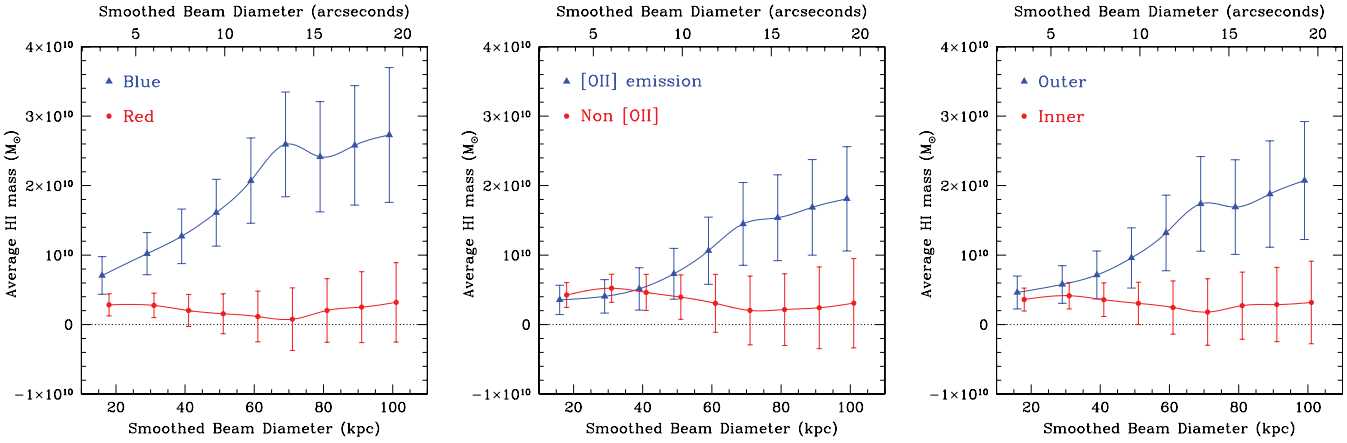

Figure 12. This figure shows the average H I mass as measured in the different smoothed synthesized beam size data for various galaxy subsamples. The left-hand panel shows the blue and red subsamples, the middle panel shows the [O II] emission and non-[O II] emission subsamples, and the right-hand panel shows the inner and outer subsamples. The points in each panel for the two subsamples have been slightly offset in the *x*-direction to prevent obscuration by overlapping values.

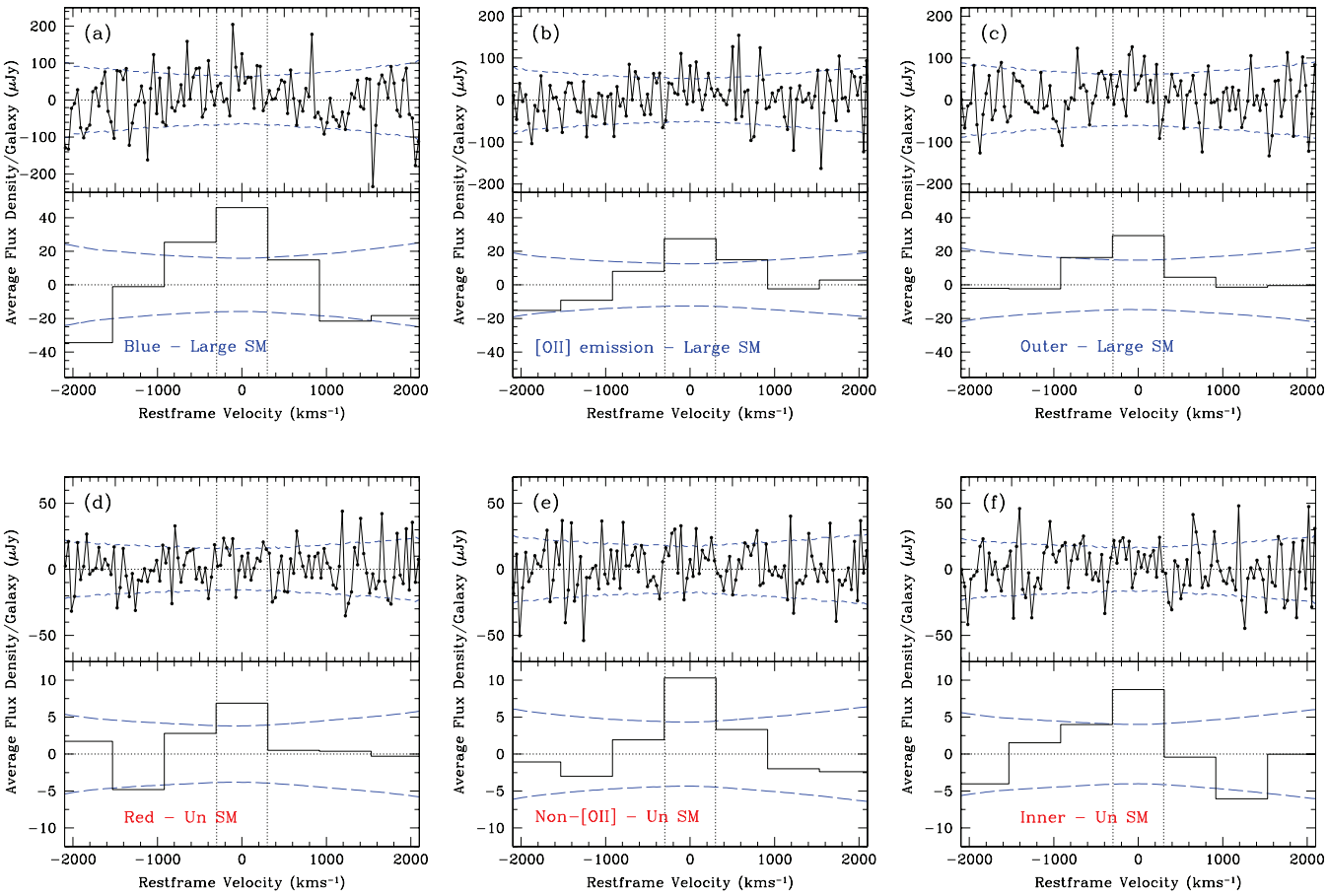

Figure 13. The average H I galaxy spectrum created from co-adding the signal of galaxies in different subsamples. The top panels use the large smoothing criterion; the bottom panels the unsmoothed criterion. Panel (a) is for the 105 blue galaxies, panel (b) is for the 168 [O II] emission galaxies and the panel (c) is for those 214 outer galaxies (those away from the cluster centre). Panel (d) is for the 219 red galaxies, panel (e) for the 156 non-[O II] emission galaxies and panel (f) is for the 110 inner galaxies (those close to the cluster centre). In each subwindow, the top spectrum has no smoothing or binning and has a velocity step size of 36.0 km s^{-1} . The bottom spectrum in each subwindow has been binned to 600 km s^{-1} . This is the velocity width that the combined H I signal of the galaxies is expected to span. For both spectra, the 1σ error is shown as dashed lines above and below zero. Note that the *y*-axis scale for the top and bottom panels is substantially different.

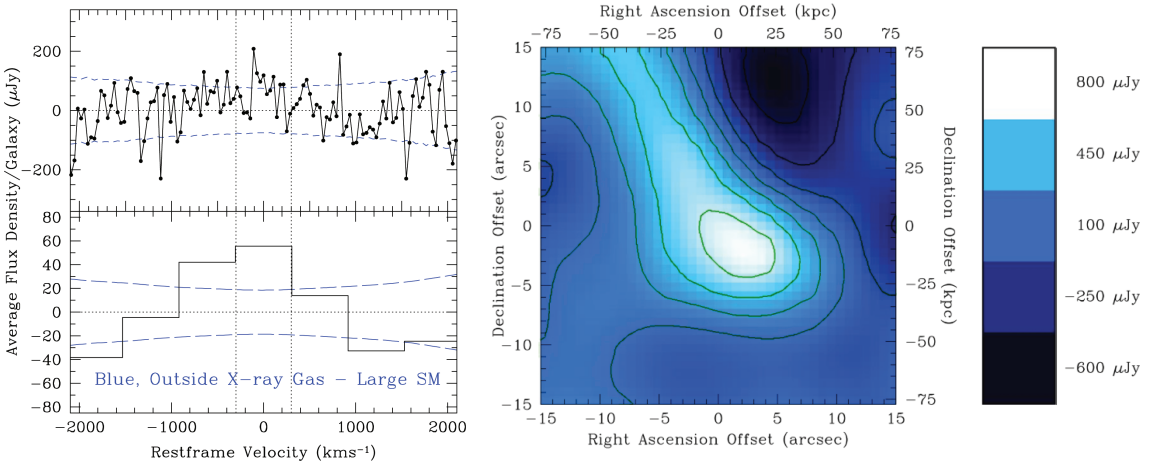

Figure 14. The left-hand panel shows the average H I galaxy spectrum created from co-adding the signal of the 94 blue galaxies outside the intracluster, X-ray gas using the large smoothing criteria. The top spectrum has no smoothing or binning and has a velocity step size of 36.0 km s^{-1} . The bottom spectrum has been binned to 600 km s^{-1} . This is the velocity width that the combined H I signal of the galaxies is expected to span. For both spectra, the 1σ error is shown as dashed lines above and below zero. The right-hand panel shows the average H I image made by co-adding the data cube around each of the blue galaxies outside the intracluster, X-ray gas and binning across 17 spectral channels (600 km s^{-1}). The radio data used for this image are that smoothed to a synthesized beam size of 9.7 arcsec (50 kpc at $z = 0.373$). The image size is shown in both arcsec and in kpc on the opposite axes. The contour levels are −500, −300, −100, 100, 300, 500 and 700 μJy.

5.2 The [O II] and non-[O II] emission subsamples

Subsamples of the Abell 370 galaxies were made based on the presence or lack of the [O II]λ3727 optical emission line in their spectra. A measured [O II] equivalent width of 5 Å was used as the cut-off between the emission and non-emission subsamples (see Section 2.3). Multiple H I mass measurements for each subsample were made, as previously, and the results are shown in Fig. 11. Unlike the red and blue galaxies, these two subsamples seem to have similar average H I gas masses in the inner regions of the galaxies. It is in measurements including the outer regions that a difference between the two subsamples can be seen. The large smoothing with the [O II] emission subsample shows an increase in the average H I gas content, while the non-[O II] emission subsample measurement is consistent with no increase in H I gas. The 168 [O II] emission galaxies have an average H I mass of $(11.4 \pm 5.2) \times 10^9$ M$_\odot$ using the large smoothing criteria while 156 non-[O II] emission galaxies have only $(4.3 \pm 1.8) \times 10^9$ using the unsmoothed criteria. The H I spectrum for the [O II] emission galaxies using the large smoothing criteria can be seen in panel (b) of Fig. 13 and the H I spectrum for the non-[O II] emission galaxies using the unsmoothed criteria in panel (e) of this figure.

The H I gas distribution in these subsamples can be seen in greater detail in the middle panel of Fig. 12. This figure shows the change in H I mass as a function of smoothed synthesized beam size for the [O II] emission and non-[O II] emission subsamples of galaxies. The two subsamples start out with similar average H I masses within the smaller synthesized beams, until they diverge at ∼50 kpc beam size. The measurements for the non-[O II] emission subsample are consistent with no increase in H I content factoring in the increasing size of the measurement errors. The [O II] emission subsample shows an increase in the H I gas content in the outskirts of the galaxies (an increase in signal in the higher beam measurements) that is similar to that seen in the blue galaxy subsample.

This similarity brings up the obvious question of how much overlap there is between the blue galaxy subsample and the [O II] emission galaxy subsample. In the [O II] emission subsample of 168 galaxies, roughly half are blue and the other half red (81 blue versus 87 red galaxies). This is the majority of the blue galaxies (there are only 24 blue galaxies in the non-[O II] emission subsample), but less than half of the total red galaxies. This shows that the [O II] subsamples are a substantially different grouping of galaxies than the blue/red galaxy subsamples (for more on the overlap of the subsamples, see Section 2.4).

The [O II] emission galaxies were broken up further into their blue and red galaxy subsamples and the average H I mass with smoothed synthesized beam size measured as seen in the left-hand panel of Fig. 15. Although we are pushing the data to its limit, a clear difference can be seen. In general, the blue [O II] emission galaxies have an average higher H I gas content than the red [O II] emission galaxies. The measured H I content of both subsamples increases with increasing synthesized beam sizes. However, the red galaxies have H I gas values consistent with zero H I gas in their inner regions (the lower synthesized beam measurements). It is only as one moves to the higher synthesized beam measurements that any H I signal appears (at low significance). From these data, one could suggest that the red [O II] emission subsample is the galaxies that have a large, optically bright, red bulge with little or no gas surrounded by optically faint disc containing some gas, i.e. similar to Hubble type 'Sa' galaxies. The resolution of the optical imaging is not sufficient to confirm this large bulge, small disc model for these galaxies. 'Sa' galaxies in the nearby Universe have median $B - V$ colour of 0.78 (Roberts & Haynes 1994), which is consistent with the colour value for the red [O II] emission galaxies (see Fig. 6, the middle, centre panel).

Similarly, the non-[O II] emission galaxies have been divided into their blue and red galaxies. Of the 156 non-[O II] emission galaxies, there are 132 red galaxies and only 24 blue galaxies. The average H I mass with smoothed synthesized beam size has been measured for these subsamples of galaxies as seen in the right-hand panel of Fig. 15. The blue non-[O II] emission galaxies appear to contain substantial amounts of H I gas with an average ∼40 × 10^9 M$_\odot$, twice that found in the blue galaxies as a whole. This result should be judged with caution as we are looking at subsample of only 24 galaxies with large measurement errors. No single galaxy or small subgroup of galaxies in this sample dominates the measured

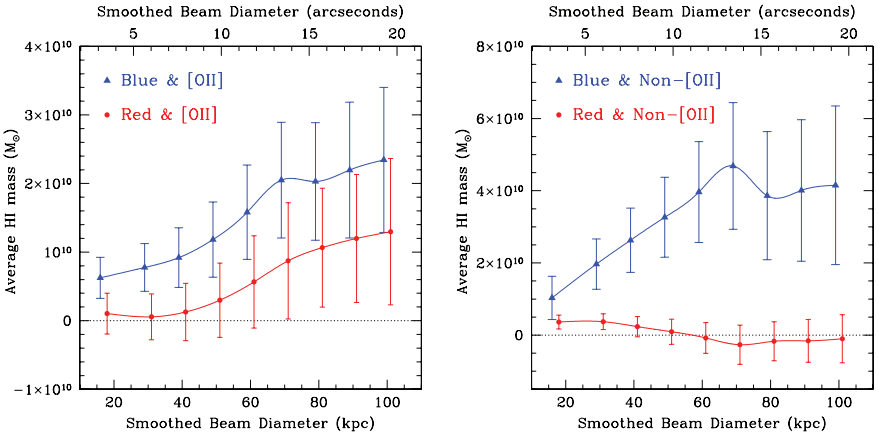

Figure 15. This figure shows the average H I mass measured in the different smoothed synthesized beam size data for the [O II] emission and non-[O II] emission subsamples split further into their constituent red and blue galaxies. The left-hand panel shows the 168 [O II] emission galaxies split up into the 87 red and 81 blue galaxies. The right-hand panel shows the 156 non-[O II] emission galaxies split into the 132 red and 24 blue galaxies. The points in each panel for the two subsamples have been slightly offset in the *x*-direction to prevent obscuration by overlapping values. Note that *y*-axis scale is substantially different between the two panels.

H I signal. Of these blue non-emission galaxies, only three lie within the R_{200} radius of the cluster. These galaxies span the complete spread of the *B*-band total absolute magnitudes of all blue galaxies in the sample (from −22.8 to −19.9). The [O II] emission line in these galaxies could be present at a very weak level, i.e. below 5 Å. It is unlikely though that the line is obscured completely by dust extinction internal to the galaxies. If this was the case, the galaxies would show a redder colour. These galaxies could be similar to E+A galaxies that have no O and B stars to create the emission lines in H II regions but contain sufficient A and F stars to give the galaxies a blue colour. Unfortunately, for these galaxies the optical spectra are not of sufficient quality to use the Hδ and Hγ absorption features to identify whether they are E+A galaxies. The lack of [O II] emission lines suggests that the galaxies currently lack strong internal ionizing radiation. Without this radiation, H II gas in the galaxies could recombine to give the higher H I content. This H II gas could be gas ionized in the previous star formation period (possibly during a starburst) or could be gas currently infalling on to the galaxy.

Although the blue non-[O II] emission galaxies appear to have a strong H I signal when considered alone, they do not dominate the total H I signal of all non-[O II] emission galaxies. The red non-[O II] emission galaxies dominate the average H I signal from all the non-[O II] emission galaxies due to their large number and their higher weight in the co-added signal, as many are located near the cluster centre and hence close to the GMRT pointing centre. In the right-hand panel of Fig. 15, the red non-[O II] emission measurements are actually quite similar to the values found for both the red galaxies and the non-[O II] emission galaxies as a whole (see the left-hand and middle panels of Fig. 12). The red non-[O II] emission sample has a measured average H I mass of $(3.6 \pm 1.9) \times 10^9\,M_\odot$ in the unsmoothed data, not dissimilar to both the total red subsample and total non-[O II] emission sample values (see Table 2).

5.3 The inner and outer cluster subsamples

Subsamples of the Abell 370 galaxies were made based on their location relative to the centre of the cluster. An inner subsample was formed from galaxies that fell within a projected distance of 2.57 Mpc (the R_{200} radius) of the cluster centre and in the redshift range $z = 0.356$–0.390 around the cluster redshift centre (see Section 2.4). Galaxies outside these criteria make up the outer galaxy subsample.

For these subsamples, H I measurements were made as previously, and the results are shown in Fig. 11. The inner subsample of galaxies has an average H I mass similar to the red galaxy subsample; any H I gas content they have is located in the central regions of the galaxies. The 110 inner galaxies have an unsmoothed average H I mass measurement of $(3.6 \pm 1.7) \times 10^9\,M_\odot$. The similarity with the red galaxies is not surprising as the inner sample is dominated by red galaxies (87 out of 110 galaxies). The H I measurements for the outer subsample are similar to that seen for the blue galaxies. There is a definite H I signal from the central regions of the galaxies with an increased H I signal when including the outskirts of the galaxies. The 219 outer galaxies have an average H I mass of $(12.1 \pm 6.1) \times 10^9\,M_\odot$ using the large smoothing criteria. The outer sample is made up of 132 red and 82 blue galaxies (this is ∼80 per cent of all the blue galaxies around Abell 370). Around two-third of the outer subsample H I signal is due to the blue galaxies with the final third coming from the outer red galaxies.

The galaxies within the inner regions of the cluster Abell 370 at $z = 0.37$ have a lower average H I mass than galaxies outside this region, following the environmental trend seen in nearby clusters. The difference in the way the H I gas is distributed in the inner and outer galaxies can be seen in greater detail in the right-hand panel of Fig. 12 which traces the change in H I mass as a function of smoothed synthesized beam size for these subsamples. The H I spectrum for the outer galaxies using the large smoothing criterion can be seen in panel (c) of Fig. 13 and the H I spectrum for the inner galaxies using the unsmoothed criterion in panel (f) of this figure.

Any H I gas located in the inner galaxy subsample seems to be concentrated in the centre of the galaxies. The central region of a galaxy is the place where H I gas could survive for longer. Only a small percentage of the interstellar medium (ISM) in a galaxy needs to be neutral to greatly reduce the ionizing flux that reaches the central regions of the galaxy. Gas in the central regions would be packed into a small volume giving rise to higher gas densities. This would allow for the H I gas to recombine faster after being ionized, extending its lifetime. Additionally, H I gas in the centre of a galaxy would also be less affected by ram pressure stripping and galaxy harassment lying deep in the gravitational well of the galaxy. In fact, galaxy harassment may actually encourage gas in

the outskirts of a galaxy to move towards the centre of the galaxy. In the simulations of Moore et al. (1996), galaxy harassment had the effect of stripping ∼10 per cent of a galaxy's gas content while the other 90 per cent of the gas sank to the inner few hundred parsec. Such an effect could be important in creating the H I gas distribution seen in the Abell 370 galaxies.

6 COMPARISON OF THE H I MEASUREMENTS WITH THE LITERATURE

Abell 370 is a large galaxy cluster with a velocity dispersion of 1263 ± 99 km s^{-1}. In the nearby Universe, there are few galaxy clusters of this size, which limit the available literature H I 21 cm emission observations for direct comparison. Table 3 lists the cluster properties of Abell 370 and three nearby clusters that have extensive literature H I observations. Abell 370 and the nearby Coma cluster have similar cluster velocity dispersions and similar X-ray gas temperatures for the hot intracluster gas in their cores. This indicates that the two clusters have similar total masses, assuming that they are both dynamically relaxed. Coma and Abell 370 are also similar, in that they both have two cD galaxies rather than the usual one seen in rich clusters. Abell 370 is substantially more massive than the other two clusters listed in the table, Abell 1367 (also known as the Leo cluster) and the Virgo cluster. Detailed comparisons of the H I gas content in Abell 370 and these clusters are discussed below.

6.1 H I density

It is necessary to compare the H I measurements of the galaxies in Abell 370 with local samples in order to quantify any evolution in the H I gas over the past ∼4 billion years (since $z = 0.37$). One way to quantify the gas evolution in Abell 370 is to compare the H I density around the cluster with values from the literature. The H I densities calculated for a variety of subsamples and volumes around Abell 370 along with various literature values can be found in Table 4 and can be seen plotted in Fig. 16. The H I density in a volume can be calculated using

$$\rho_{\rm H\,I} = \frac{n_{\rm gal}\overline{M}_{\rm H\,I}}{V}, \tag{3}$$

where $\rho_{\rm H\,I}$ is the H I density, $n_{\rm gal}$ is the number of galaxies being considered, $\overline{M}_{\rm H\,I}$ is the average H I mass measured for these galaxies and V is the volume in which these galaxies are contained.

The comoving volume containing all 324 Abell 370 galaxies was calculated from the extent of the optical imaging (see Fig. 1) and the redshift range spanned by the galaxies. The total area on the sky of the optical imaging after accounting for the removal of the exclusion regions (see Fig. 1) is 0.776 deg^2. Not all this area has uniform optical sampling which may cause a slight underestimate of the H I densities measured. Taking into account the limits placed by the GMRT 10 per cent beam level, the area on the sky containing the galaxies with H I measurements is 0.668 deg^2. The H I frequency range of the GMRT observations spans from $z = 0.345$ to 0.387. Using these values, the total comoving volume of the Abell 370 H I measurements is 62 300 Mpc^3. The volume is much longer in the redshift direction than in projected distance on the sky (at most ∼15 Mpc across compared to 148 Mpc deep).

Using this volume, an H I density of $(0.034 \pm 0.018) \times 10^9$ M$_\odot$ Mpc^{-3} is found using all 324 Abell 370 galaxies. The H I density in this volume due to just the 105 blue galaxies is $(0.032 \pm 0.011) \times 10^9$ M$_\odot$ Mpc^{-3}. This almost equals the density calculated for all the galaxies, indicating that most of the H I gas around the cluster is located in the blue galaxies. In contrast, the H I density due to just the 219 red galaxies is $(0.0098 \pm 0.0056) \times 10^9$ M$_\odot$ Mpc^{-3}. The blue and red galaxy values do not sum exactly to give the H I density from all galaxies due to the weighting schemes used when measuring the H I gas. The H I density measured using only the 168 [O II] emission galaxies is $(0.031 \pm 0.014) \times 10^9$ M$_\odot$ Mpc^{-3}. This is similar to that found for the blue galaxies, which shows that this sample also selects the majority of the H I gas in galaxies within this volume.

The H I density measurements listed above only include the H I gas contained in the known Abell 370 galaxies; they do not take into account the many 'missing', optically fainter galaxies in the volume that may contain H I gas. As such these measurements are only lower limits on the total H I density in the volume. These previously measured values have been scaled up to an estimate of the total H I density in the volume. This is done by assuming that the optical luminosity density of the galaxies is proportional to their H I density. The optical luminosity density in the B band for the galaxies in each Abell 370 galaxy sample was measured. For each of the galaxy samples, a Schechter function fit using χ^2 minimization was made to their magnitude distribution. In this function fitting, the faint-end slope of the luminosity function, α, was set at 1.35 ± 0.10 because the Abell 370 B-band magnitudes do not extend faint enough to allow an accurate determination of this parameter. This α value is based on the literature results for H I galaxies in the HIPASS (Zwaan et al. 2005) and optical cluster galaxies in the 2dF Galaxy Redshift Survey (De Propris et al. 2003). The fitted Schechter functions were integrated over all magnitudes to create an estimate of the total optical luminosity density of the galaxies. The H I density for each galaxy sample was then scaled up by the ratio of this total

Table 3. The cluster properties of Abell 370 and some nearby clusters. The cluster velocity dispersion of Abell 370 is measured from the redshifts obtain in this work (Pracy et al., in preparation). The luminosity distance for Abell 370 and Abell 1367 has been calculated from their redshift. For the Coma and Virgo clusters, the luminosity distance is the value found in the GOLDMINE data base (Gavazzi et al. 2003). The X-ray temperature data and other velocity dispersion measurements are from the compilation by Wu et al. (1999). The R_{200} values are calculated from the velocity dispersions.

Galaxy cluster	Redshift	Luminosity distance (Mpc)	X-ray gas temperature $kT_{\rm X}$ (eV)	Velocity dispersion (km s^{-1})	R_{200} (Mpc)
Abell 370	0.373	2000	7.13 ± 1.05	1263^{+99}_{-99}	$2.57^{+0.20}_{-0.20}$
Coma cluster	0.023	96.0	8.38 ± 0.34	1010^{+51}_{-49}	$2.47^{+0.12}_{-0.12}$
Abell 1367	0.022	91.3	3.50 ± 0.18	822^{+69}_{-55}	$2.01^{+0.17}_{-0.13}$
Virgo cluster	0.0036	17.0	2.20 ± 0.69	673^{+48}_{-40}	$1.66^{+0.12}_{-0.10}$

Table 4. This table lists the H I gas density measured in different subsamples of galaxies around Abell 370, including extrapolations to the total H I density. Included in the table are also a number of literature values for the cosmic H I gas density at a few different redshifts and the H I gas density found in nearby galaxy clusters. The volume for which the H I density is measured is listed where relevant.

Galaxy sample	H I gas density (10^9 $M_\odot$ Mpc^{-3})		Volume (Mpc^3)	Number of Galaxies
Abell 370 samples				
All Galaxies	0.034	±0.018	62 300	324
Blue Galaxies	0.032	±0.011	62 300	105
[O II] emission Galaxies	0.031	±0.014	62 300	168
Red Galaxies	0.0098	±0.0056	62 300	219
All Galaxies – *extrapolated* (×2.18 ± 0.58)	0.075	±0.044	62 300	324+
Blue galaxies – *extrapolated* (×2.13 ± 0.61)	0.068	±0.030	62 300	105+
Inner Galaxies	5.6	±2.6	71	110
Galaxies within 8 Mpc	0.53	±0.38	2140	220
Blue Galaxies within 8 Mpc	0.47	±0.20	2140	58
Literature samples				
Cosmic density $z = 0$: H I 21 cm (Zwaan et al. 2005)	0.0510	±0.0083	–	4315
Cosmic density $z = 0.24$: H I 21 cm (Lah et al. 2007)	0.095	±0.044	–	121
Cosmic density $z \sim 0.6$: DLAs[a] (Rao et al. 2006)	0.100	±0.037	–	18
Cosmic density $z \sim 3.7$: DLAs (Prochaska et al. 2005)	0.111	±0.018	–	89
Virgo cluster within 2.5 Mpc (GOLDMINE)	2.23	–	65	252
Abell 1367 within 2.5 Mpc (Cortese et al. 2008)	1.066	±0.019	65	36
Coma cluster within 2.5 Mpc (GOLDMINE)	0.74	–	65	22
Coma cluster within 8 Mpc (GOLDMINE)	0.066	–	2140	42

[a]Damped Lyman-α absorption systems.

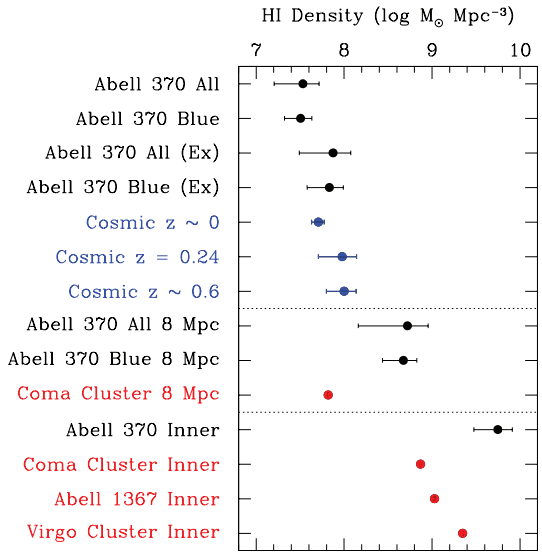

Figure 16. This figure shows the measured H I gas density around Abell 370 for various subsamples and that found in a variety of literature samples. The figure is divided into three parts by faint dashed lines. The top part shows measurements made from the total volume sampled around Abell 370 in this work. It includes the H I density measured from just the known Abell 370 galaxies as well as extrapolations to the total H I density in the volume (the 'Ex' values). Also shown in the top part are cosmic H I density values at variety of redshifts. The middle part shows the H I density within 8 Mpc of the cluster centre of Abell 370 and a similar-sized volume around the nearby Coma cluster. The bottom part shows the H I density within ∼2.5 Mpc of the cluster centre of Abell 370 and in similar volumes within nearby galaxy clusters.

optical luminosity density to the optical luminosity density measured from just the galaxies in the sample. These total H I density estimates are the extrapolated values listed in Table 4 and are shown in Fig. 16. The value of this ratio is listed in brackets in the table, next to the sample name.

Also measured was the H I density for the 110 inner galaxies in Abell 370, i.e. the H I density within the cluster core. When calculating the inner density, the average H I mass from the unsmoothed measurement was used because this has the highest precision and appears to contain the total H I signal for these galaxies (see Section 5.3). The galaxies in this inner subsample span a projected distance on the sky of $R_{200} = 2.57$ Mpc from the cluster centre and a redshift range of $z = 0.357$–0.387, a cosmological distance of 106 Mpc. However, these galaxies close to the cluster core have large peculiar motions. As such the majority of these galaxies are likely to span a much smaller distance in the redshift direction than that indicated by this direct cosmological distance conversion. A reasonable assumed distance that the majority of the inner galaxies would span in the redshift direction would be 2.57 Mpc, i.e. similar to the galaxies projected distance on the sky. This is the physical volume spanned by the galaxies which should remain unchanged with time in this gravitationally bound region. Using this value, the volume probed is 71 Mpc^3, which makes the H I density in this region $(5.6 \pm 2.6) \times 10^9$ $M_\odot$ Mpc^{-3}.

The H I density measured for the inner subsample is substantially greater (more than 50 times higher) than even the extrapolated H I densities measured for the other galaxy samples in Abell 370. Even though the galaxies in the cluster core may have lower H I gas content than similar galaxies in the field, they are packed into a very small volume, dramatically raising the H I density measured there. Galaxies in field environments may have more H I gas per galaxy,

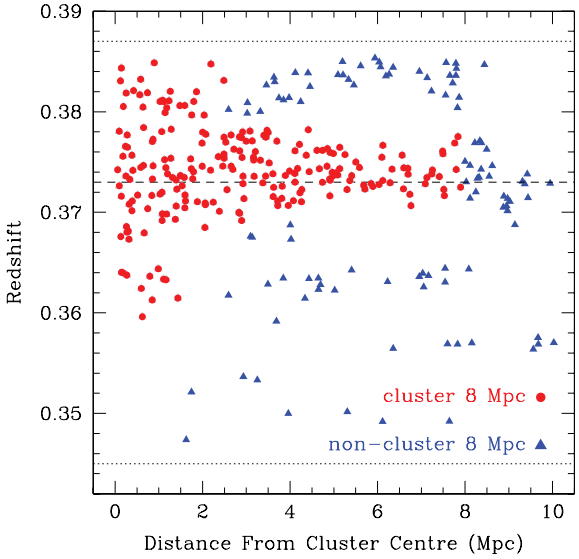

Figure 17. This figure shows the redshift versus projected distance from the cluster centre for all 324 galaxies used in the H I co-adding. The circular points are those galaxies expected to lie within 8 Mpc of the cluster centre both in projected distance and in the redshift direction after taking into account the galaxies peculiar motion. The triangular points are those galaxies expected to lie further away than 8 Mpc. The two dotted lines are the frequency limits of the GMRT and the dashed line is the redshift of the cluster centre.

but they are spread over larger volumes reducing the H I density found there.

In order to make a comparison with the nearby galaxy cluster of Coma, a sample of galaxies within 8 Mpc of the cluster centre of Abell 370 was selected. Fig. 17 shows the redshifts of the Abell 370 galaxies plotted against their projected distance from the cluster centre. Galaxies close to the cluster core have larger peculiar velocities than those further out. Using this fact, an envelop was drawn in the figure consisting of smoothly varying curves that is the locus boundary for those galaxies likely to lie within 8 Mpc of the cluster centre; these are the 220 circular points in Fig. 17. These galaxies are assumed to all lie within the 8 Mpc radius sphere centred on the cluster core with physical volume 2140 Mpc^3 (again the volume spanned by these galaxies should remain relatively unchanged with time in this gravitationally bound region). The average H I mass measured for these galaxies is listed in Table 2, as is the values for the subsample of 58 blue galaxies within this selection. Using the large smoothing average H I mass measurement of all 220 galaxies, an H I density of $(0.53 \pm 0.38) \times 10^9\,\mathrm{M}_\odot\,\mathrm{Mpc}^{-3}$ is found (this is the value plotted in Fig. 16 and listed in Table 4). Using the unsmoothed average H I mass measurement, an H I density of $(0.37 \pm 0.14) \times 10^9\,\mathrm{M}_\odot\,\mathrm{Mpc}^{-3}$ is found, which has substantially higher signal to noise. If one considers only the 58 blue galaxies in this region, using their average H I mass large smoothing measurement, an H I density of $(0.47 \pm 0.20) \times 10^9\,\mathrm{M}_\odot\,\mathrm{Mpc}^{-3}$ is found. This is comparable to that measured for all 220 galaxies in the selected 8 Mpc radius region which suggests that again it is the blue galaxies that contain the majority of the H I gas within this volume.

The first set of literature values listed in Table 4 is H I gas cosmic density values at a variety of redshifts. These values were all converted to the H I densities; some were published as neutral gas densities and included a correction for the neutral helium content. The first value listed is the $z = 0$ cosmic H I density as measured in the HIPASS survey (Zwaan et al. 2005) using H I 21 cm emission from a large sample of galaxies across the entire southern sky. The second value is the H I density measured in a sample of star-forming galaxies at $z = 0.24$ using co-added H I 21 cm emission (Lah et al. 2007). The other two values are from damped Lyα measurements, looking at the H I absorption in quasar spectra in the rest-frame ultraviolet. The lower redshift value is from damped Lyα absorbers at redshifts $z \sim 0.6$ (redshift range $z = 0.1$–0.9) that have been optically selected to have Mg II absorption, before being followed up in the ultraviolet with the *Hubble Space Telescope* (Rao, Turnshek & Nestor 2006). The $z \sim 3.7$ (redshift range $z = 3.5$–4.0) value has been measured from optical spectra of quasars primarily from the Sloan Digital Sky Survey (the Lyα absorption is redshifted into the optical at these redshifts) (Prochaska, Herbert-Fort & Wolfe 2005).

The listed cosmic H I density values beyond redshift $z = 0$ are similar. They are all around $0.10 \times 10^9\,\mathrm{M}_\odot\,\mathrm{Mpc}^{-3}$, which is twice the H I density at $z = 0$. The $z = 0.24$ and $z \sim 0.6$ values are the cosmic density measurements which are closest in the redshift to Abell 370 at $z = 0.37$. They are plotted with the $z = 0$ in the top part of Fig. 16. The $z \sim 3.7$ value is the highest H I cosmic density value as currently measured. The H I density measured in the larger volume samples of Abell 370 galaxies is slightly less than the H I cosmic density found at $z = 0$ (see the top part of Fig. 16). However, the extrapolated H I density values are comparable to the H I cosmic density found at $z = 0.24$ and $z \sim 0.6$. The errors in these measurements make it difficult to determine if there has been any substantial evolution in the H I gas in galaxies from these values. Indeed it is probably not fair to compare the H I density found in this large volume around Abell 370 to the cosmic density as we are dealing with an unusual volume of the Universe with a considerably higher galaxy density than the average. Additionally, the extrapolation used to scale up the H I gas density is highly uncertain particularly in the inner regions of the cluster where the high galaxy density would probably affect the smaller galaxies gas content more significantly than the larger galaxies. To do a fair test for evolution, it is necessary to compare the measured H I density around Abell 370 to nearby volumes with similarly high galaxy densities.

The second set of literature values listed in Table 4 is derived from H I density values for three nearby galaxy clusters. The first value is for the Virgo cluster which has H I observations from Gavazzi et al. (2005) which are available from the GOLDMINE data base (Gavazzi et al. 2003). These include targeted observations of all late-type galaxies with $m_\mathrm{p} \leq 18.0$ mag, which at the distance of the cluster is more than 6 mag fainter than the Abell 370 observations. There are 252 galaxies with H I measurements within a radius 2.5 Mpc in the inner regions of the Virgo cluster. For this volume, an H I density of $2.23 \times 10^9\,\mathrm{M}_\odot\,\mathrm{Mpc}^{-3}$ was measured. This measurement is a lower limit as it does not include a correction for any missing galaxies. However, it is likely to be close to the total H I density as it contains the majority of the galaxies with significant H I gas content.

The second galaxy cluster considered is Abell 1367 which has H I observations from the Arecibo Galaxy Environment Survey (AGES), a blind H I survey (Cortese et al. 2008). Using these data, the H I density within a radius 2.5 Mpc around the cluster centre was measured. Galaxies were included in this volume if they lie within the 2.5 Mpc projected distance of the sky of the cluster centre and had redshifts between 4000 and 9000 $\mathrm{km\,s}^{-1}$. There are 36 galaxies with H I measurements not contaminated by radio frequency interference (RFI) in this region which gives an H I density of $(1.066 \pm 0.0192) \times 10^9\,\mathrm{M}_\odot\,\mathrm{Mpc}^{-3}$.

The third galaxy cluster considered is the Coma cluster. The H I observations came from Gavazzi et al. (2006) and are compiled with optical data in the GOLDMINE data base (Gavazzi et al. 2003). The

H I observations include 94 per cent of all late-type galaxies with apparent magnitude $m_p \leq 15.7$ mag in the Coma supercluster (a much larger region surrounding the Coma cluster). This magnitude limit is equivalent to B-band absolute magnitude of ~ -19.2 at the distance of Coma cluster (the faintest Abell 370 galaxy is -19.7). The H I density was measured around the Coma cluster centre out to a radius of 2.5 and 8 Mpc. A radius of 8 Mpc is the maximum projected distance from the Coma cluster with good observations (there were insufficient H I observations to make similar 8 Mpc measurements for Abell 1367 and the Virgo cluster). The inner 2.5 Mpc radius region of the Coma cluster has an H I density of $0.74 \times 10^9\,M_\odot\,Mpc^{-3}$ from 22 H I galaxies. The larger 8 Mpc radius region of the Coma cluster has an H I density of $0.066 \times 10^9\,M_\odot\,Mpc^{-3}$ from 42 H I galaxies.

The inner values for Abell 370 and the three literature clusters are shown together in the bottom part of Fig. 16. These inner samples all come from similar-sized volumes, spheres with radii $\sim$2.5 Mpc. The R_{200} radius for Coma and Abell 370 is close to this value, but Abell 1367 has an R_{200} radius of $2.01^{+0.17}_{-0.13}$ Mpc and the Virgo cluster of $1.66^{+0.12}_{-0.10}$ Mpc (see Table 3). The H I density within the R_{200} radii for these two smaller clusters is almost twice as high in both cases. As can be seen in bottom part of Fig. 16 in the nearby cluster values, the H I density increases with decreasing cluster size. The H I density in the inner Coma region is three times smaller than that found in the smaller irregular Virgo cluster, with the H I density of Abell 1367 in between. This clearly shows the known trend in the nearby Universe that H I gas in galaxies is lower in high-galaxy-density environments. The H I density found for Abell 370 is approximately three times higher than that found in Virgo and approximately eight times higher than that found in Coma, a similar-sized cluster. This is not evidence against the trend of H I gas in galaxies being lower in high-galaxy-density environments. This trend is seen for the Abell 370 galaxies when comparing the inner and outer subsamples (see Section 5.3). Rather this high H I density value found in the inner regions of Abell 370 compared to nearby clusters is an indication that there has been substantial evolution in the gas content of galaxies in clusters over the last $\sim$4 billion years since $z = 0.37$.

Similarly, the region within 8 Mpc of the centre of Abell 370 has an H I density that is approximately eight times higher than the similar-sized region around Coma. This is a statistically significant difference as can be seen in the middle part of Fig. 16 (the Coma value has no discernible random error). As Coma and Abell 370 are galaxy clusters of similar size, this is again evidence of substantial evolution in the gas content of cluster galaxies between redshift $z = 0.37$ and the present.

In order to ensure that the striking differences between the H I densities found for the Coma cluster and Abell 370 are real one must ensure that there is no significant biases on the measurements that could be distorting the result. The Coma H I gas measurements come from targeted observations rather than a blind H I search of the cluster. As such it is not impossible that an appreciable fraction of the H I gas in galaxies within the cluster has been missed. This is unlikely though, as all the optically bright late-type galaxies have been observed and these are likely to be the dominate contributors to the H I density. Even if including the missing low H I mass galaxies raises the H I density in Coma by a factor of 2, there is still considerably more gas found around Abell 370. The unaccounted for gas due to these smaller galaxies is unlikely to be anywhere near as substantially as this particular as these galaxies with lower total galaxy masses will have a harder time holding on to their gas against the high-density environmental mechanisms, such as ram pressure stripping. Additionally, it is likely that an appreciable amount of the H I gas is missing in the Abell 370 volumes due to the relatively bright optical magnitude limit of this galaxy sample.

The optical imaging of Abell 370 does not extend fully out to a projected radius of 8 Mpc in all directions as seen in Fig. 3. This will result in missing some galaxies within this volume causing a small underestimation of the H I density in this volume. To select the Coma and Virgo galaxies, the distances in the GOLDMINE data base were used. These distances have had the effect of the peculiar velocities of the galaxies removed, allowing one to select the galaxies close to the cluster centres. If these distances are incorrect for a large number of galaxies, then this could result in an underestimation of the true H I densities in these clusters. However, this is unlikely as the distances appear quite reasonable based on their redshift and spatial distribution on the sky. The literature values for the clusters included H I flux upper limits for a number of galaxies. These galaxies were considered to have no gas when doing the density calculations. They are unlikely to contain sufficient gas to significantly affect the results.

Ideally one would want deep H I blind observations of a number of large galaxy cluster at low redshift to compare with the Abell 370 observations. Such published data do not exist as yet. Due to the uncertainties on the current galaxy samples of both Abell 370 and the low-redshift clusters, it is difficult to say with precision the amount of difference in the H I densities. However, from the measurements it is clear that Abell 370 has considerably more gas than local clusters, suggesting that there has been substantial evolution in the gas content in clusters over the last 4 billion years.

The H I density of Abell 370 is markedly larger than that found in the Coma cluster in the regions considered. The H I gas density in Abell 370 is up to eight times higher than in Coma. The increase in the cosmic H I density from $z = 0$ to the largest known values at higher redshifts is at most a factor of 2 (see Table 4). If Abell 370 were to evolve into a gas-poor system like Coma in $\sim$4 billion years, then the rate of decrease in the gas would be considerably faster than the rate of decrease seen in the field. This higher rate of decrease in gas content could be caused by the combination of the higher rate of galaxy–galaxy interactions in the cluster environment and the interactions between the ISM of the galaxies with the IGM of the cluster which is denser than the IGM of the field.

6.2 Average H I mass comparisons with the Coma cluster

Comparing the H I measurements of the galaxies in Abell 370 directly with local samples is difficult, primarily due to the unusual way in which the Abell 370 measurements were made, i.e. by co-adding the H I 21 cm emission signal from multiple galaxies. One way of doing this comparison is to make similar co-added average H I mass measurements in nearby clusters using literature H I 21 cm emission values. To do this, one needs a complete sample of the optical galaxies in a nearby cluster down to the magnitude limits of the Abell 370 galaxy sample. Additionally, one needs to know the H I mass for each of these optical galaxies. Each galaxy in the Abell 370 sample can then be randomly matched to a literature galaxy in the nearby cluster with similar absolute optical magnitude. The average H I mass of this randomly matched sample of literature galaxies can then be calculated. This can be repeated multiple times, each time taking different randomly matched samples. The different random samples are then combined to give a robust measure of the average H I mass for a sample of galaxies with similar optical magnitude distributions to the Abell 370 galaxies. The variation between the different random samplings provides an estimate on the error in this measurement.

This comparison was done using galaxies in the nearby Coma cluster as the GOLDMINE data base contains both optical and H I observations for the galaxies (Gavazzi et al. 2003) (see above for details on this galaxy sample). Each galaxy in the Abell 370 sample was matched to a random Coma galaxy with *B*-band absolute magnitude within 0.25 mag.

The Coma data were used to make average H I mass measurements to compare with the Abell 370 measurements for all 324 galaxies, for the inner and outer subsamples. Galaxies that lie within 8.0 Mpc of the cluster centre of Coma were chosen to match against all 324 Abell 370 galaxies. In this Coma cluster sample, there were 113 galaxies within the magnitude range spanned by the 324 Abell 370 galaxies. Of these, 24 per cent had detected H I masses. The galaxies within a radius of 2.5 Mpc of the cluster centre of Coma were matched with the inner subsample of the Abell 370 galaxies. In this Coma inner sample, there were 67 galaxies within the magnitude range of the galaxies in the Abell 370 inner sample. Of these, 19 per cent had measured H I masses. The galaxies more than 2.5 Mpc from the cluster centre of Coma, but less than 8.0 Mpc from the centre were chosen to compare with the Abell 370 outer subsample. In this Coma outer sample, there are 37 galaxies within the magnitude range of the galaxies in the Abell 370 outer sample. Of these, 35 per cent had measured H I masses. The number of Coma galaxies in each subsamples is smaller than the number of Abell 370 galaxies. As such the matched samples will contain repeats of the Coma galaxies which may introduce a bias. However, a larger sample of nearby cluster galaxies will likely have a similar distribution so that the effect of any bias will likely be small.

The measured average H I mass for the Abell 370 subsamples and the similar Coma measurements can be seen in Fig. 18. There is a similar trend in both Coma and Abell 370, that the galaxies in the outer regions of both clusters have average H I masses that are ∼3.5 times higher than that found in their inner galaxies. This is the well-known trend, that galaxies within dense cluster cores generally have less H I gas content than galaxies in lower density environments (Haynes et al. 1984). This is true in nearby clusters and appears to be true at $z = 0.37$, ∼4 billion years in the past. The similar ratio between the inner and outer measurements in the two clusters could suggest that the mechanism for creating this H I gas reduction is of similar strength in both clusters.

Despite this trend with galaxy density seen in both clusters, the amount of H I gas content of the galaxies is substantially different between the two clusters. In all three measurements, the average H I mass in the Abell 370 galaxies is ∼10 times larger than that found in the Coma samples of optical galaxies with similar magnitudes. This higher H I gas content is likely due to the optically bright, blue galaxies that exist around Abell 370 that have been shown to have large quantities of H I gas. Similar galaxies do not exist in Coma. This is seen in the difference in Butcher–Oemler blue fraction between the clusters; Abell 370 has a blue fraction of ∼0.13 while Coma has a blue fraction of ∼0.03 (Butcher & Oemler 1984), a factor of ∼4 less. The blue galaxies in Coma have had an extra ∼4 billion years of evolution to remove their H I gas through star formation or interactions in the dense galaxy environment. The young, blue stars in such galaxies would have died out in time-scales less than ∼4 billion years. Without more H I gas to supply the fuel for additional star formation, the galaxies would have dimmed and evolved to a redder colour. The passive evolution of the galaxies in Abell 370 over ∼4 billion years would decrease their *B*-band magnitudes by up to 1 mag (Poggianti 1997). Decreasing the optical brightness of the galaxies in Abell 370 by ∼1 mag creates a reasonable match to the *B*-band magnitude distribution of the Coma galaxies.

Similar average H I mass comparison with either Abell 1367 or the Virgo cluster is not practical as there are insufficient galaxies optically bright enough to match to the Abell 370 galaxies.

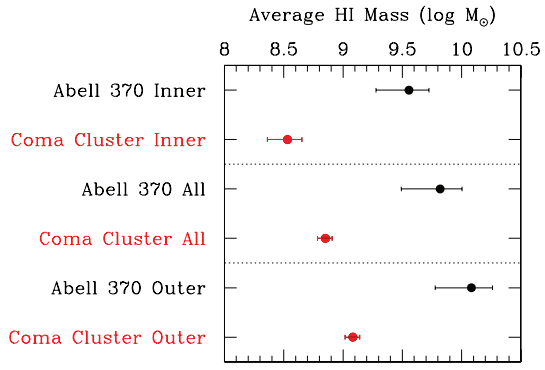

Figure 18. This figure shows the average H I mass for selected galaxy subsamples from Abell 370 and similar measurements made using literature values for the Coma cluster. The Coma average H I mass measurements are made from randomly selected samples of galaxies with similar *B*-band absolute magnitudes to the Abell 370 galaxies (see the text for details).

6.3 H I mass-to-light ratios

In the previous literature comparisons, it has been shown that the Abell 370 galaxies have higher H I gas content than galaxies in nearby clusters. This raises the question whether the Abell 370 galaxies have unusual H I gas properties compared to nearby galaxies. One way of assessing this is to measure the H I mass-to-optical-light ratios seen for the Abell 370 galaxy subsamples and compare these to 'normal' galaxy values. The average ratio of H I mass to the *B*-band luminosity for a variety of Abell 370 subsamples is shown in Fig. 19.

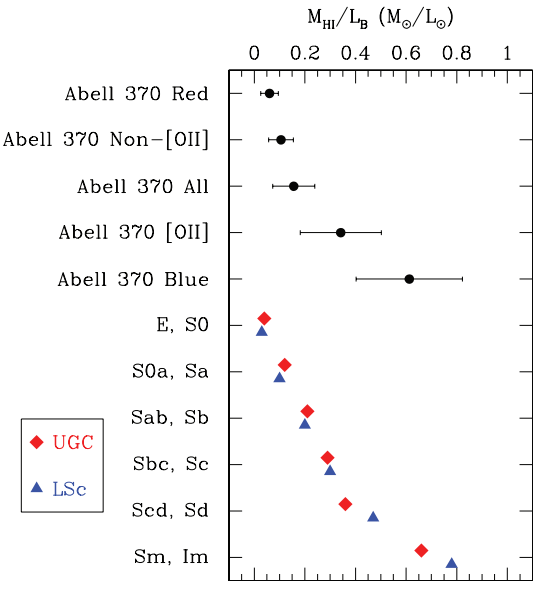

Figure 19. This figure shows the average ratio of H I mass to optical *B*-band light ratio for various subsamples of the Abell 370 galaxies. Also plotted for comparison are the median H I mass-to-light ratios for different morphological type galaxies from the UGC and the Local Super Cluster sample (LSc) (Roberts & Haynes 1994).

For each of the Abell 370 galaxy subsamples, the average rest-frame *B*-band luminosity in units of the solar luminosity was calculated using an absolute *B*-band magnitude for the sum of 5.46 (Bessell, Castelli & Plez 1998). When combining the individual galaxy *B*-band luminosities, weights were used equal to those used in the average H I mass measurements to ensure that similar quantities were measured. The weighted average and the non-weighted average *B*-band luminosities are very similar for the subsamples considered (for all 324 galaxies, the difference in values was ∼7 per cent). This suggests that the weighting scheme used in H I mass measurements does not create a bias in the results. Using this average *B*-band luminosity and the average H I mass for a subsample, the H I mass-to-light ratio can be calculated.

The literature H I mass-to-blue-light ratios considered are for samples of galaxies with different morphological types (Roberts & Haynes 1994). The morphologies move along the Hubble sequence starting with the early-type galaxies of ellipticals and S0s, moving across the variety of late-type galaxies in the direction of increasing spiral structure (moving from Sa to Sd galaxies) and finally reaching the irregular galaxies. The H I mass-to-light ratio increases fairly regularly along this sequence. These literature measurements are the median values from two catalogues, the Uppsala General Catalogue (UGC) and the Local Super Cluster sample (LSc).

In Fig. 19, the values for the galaxy subsamples of Abell 370 are plotted in the order of increasing H I mass-to-light ratio. The red galaxy subsample has the lowest H I mass-to-light ratio while the blue galaxies have the highest. Below these the literature values from both the UGC and the Local Super Cluster sample (LSc) are plotted. The red galaxy subsample has an H I mass-to-light ratio similar to that for the ellipticals and S0 galaxies of the literature samples, and the blue galaxy subsample has a ratio similar to those literature galaxies with the most spiral structure or which are irregular. Unfortunately, deriving morphologies for the galaxies in Abell 370 is not possible due to the poor seeing in the optical imaging combined with the small size of galaxies at a redshift of $z = 0.37$. However, it is clear from this comparison that galaxies in Abell 370 seem to follow similar trends in H I mass-to-light ratios as nearby, 'normal' galaxies and even have similar H I mass-to-light ratios for galaxies of roughly similar types (the red and blue galaxies). With time, the galaxies in Abell 370 will undergo passive evolution, and their optical brightness will decrease. In order for the galaxies still to have 'normal' H I mass-to-light ratios, their H I gas content will need to decrease similarly during this evolution.

7 STAR FORMATION RATE RESULTS

7.1 The SFR–H I mass correlation for the galaxies

In the local Universe, there is a reasonably strong correlation between the SFR in a galaxy and the mass of H I gas in that galaxy. This relationship can be seen in fig. 3 of Doyle & Drinkwater (2006), where they compared the H I masses of individual galaxies from the HIPASS to their SFR derived from *IRAS* infrared data. This correlation between galaxy H I mass and SFR can be examined in the galaxies around Abell 370. The star formation rate for the Abell 370 galaxies was derived from their [O II] luminosity as described in Section 2.3. In Fig. 20, the large circular point shows the comparison of the average [O II] SFR against the average H I for the Abell 370 galaxies with [O II] equivalent width greater than 5 Å (the 168 galaxies of the [O II] emission subsample). When calculating the average [O II] SFR, the same weighting scheme was used as in the average H I mass measurement. The difference between this

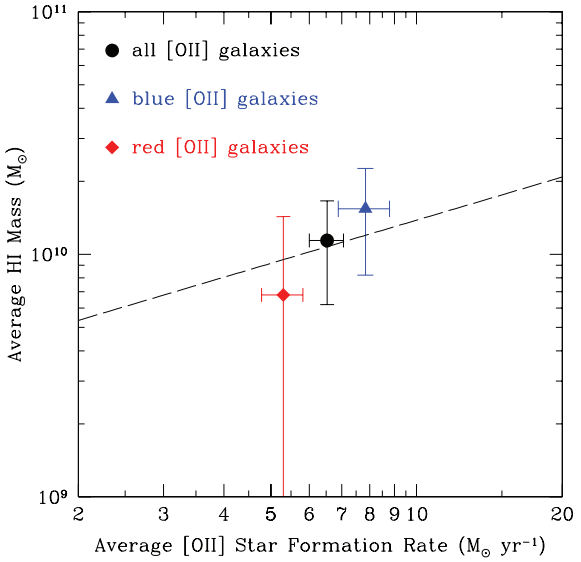

Figure 20. This figure shows the comparison of the average galaxy [O II] SFRs with their average H I mass. The dashed line is the relationship seen in $z \sim 0$ galaxies (Doyle & Drinkwater 2006). The large circular point is the average for all 168 galaxies with [O II] emission. The triangle point is the average for the 81 blue galaxies with [O II] emission. The diamond point is the average of the 87 red galaxies with [O II] emission.

weighted average SFR and the standard average is small (less than 1 per cent).

Plotted in Fig. 20 is the linear fit to the SFR–H I correlation for the local sample of galaxies (Doyle & Drinkwater 2006). The average value for the Abell 370 [O II] emission galaxies lies almost on this line. This indicates that the galaxies around Abell 370 have normal galaxy properties, in that their higher H I gas contents lead naturally to higher SFRs. The same SFR–H I correlation relationship was found to hold at $z = 0.24$ in a field sample of star-forming galaxies (Lah et al. 2007). These two results at $z = 0.24$ and 0.37 suggest that the increase in SFR densities seen at moderate redshifts is simply due to higher H I gas content in the galaxies. The good SFR–H I correlation agreement for the Abell 370 galaxies also indicates that the assumptions and corrections made when calculating the [O II] SFR were reasonable.

Also shown in Fig. 20 are the values for the average galaxy [O II] SFRs and average galaxy H I masses for the 81 galaxies that have [O II] emission and blue colours (the triangular point) as well as for the 87 galaxies that have [O II] emission but have red colours (the diamond point). Both of these measurements agree with the Doyle & Drinkwater line. The expected trend that the blue [O II] galaxies have higher SFRs and higher H I masses compared to red [O II] galaxies is seen.

From the measured SFR, it would take ∼1.7 billion years for the [O II] emission galaxies to turn all their H I gas into stars. This assumes that the conversion from H I gas to stars is 100 per cent efficient, that there is no change in the SFR as the H I gas decreases, that there is no significant amount of molecular hydrogen gas, that galaxy harassment or H I stripping has minimal effect on the gas, that there is no recycling of gas and that there is no gas accretion on to the galaxies. None of these assumptions is reasonable. However, this rough time frame does show that it is possible for the H I gas in the Abell 370 galaxies to be depleted in the ∼4 billion years from $z = 0.37$ to the current epoch. Abell 370 can easily evolve into an

H I gas-poor galaxy cluster based entirely on the SFR seen in its galaxies.

7.2 The SFR–radio continuum correlation

Synchrotron radio emission is generated in areas of active star formation from relativistic electrons accelerated in supernova remnants. The luminosity of this radiation has a good correlation with other galaxy SFR indicators. This radiation in nearby galaxies is often measured using 1.4 GHz observations and compared to SFRs measured using other indicators (Sullivan et al. 2001; Bell 2003). The GMRT data also provided measurements of the radio continuum emission at 1040 MHz for objects surrounding Abell 370. Since the Abell 370 galaxies are at a redshift of $z = 0.37$, their deredshifted radio continuum emission in the GMRT data has a frequency of 1.4 GHz. It is therefore possible to directly measure the 1.4 GHz radio continuum emission from the Abell 370 galaxies and compare it to their measured [O II] SFR to see if the correlations found in the nearby Universe hold at $z = 0.37$.

Despite the low radio continuum rms of only 20 μJy, only a handful of the 168 Abell 370 galaxies with [O II] emission has radio continuum flux densities at the 5σ level. To increase the number of galaxies studied, the signal from all 168 galaxies was co-added using their known optical position to measure their average radio continuum flux density. This co-adding was done using a similar weighted average as used in the H I measurements, to take into account the variation in noise due to the GMRT primary beam shape. Using this method, the 168 galaxies with [O II] emission have a measured average flux density of 25.7 ± 2.8 μJy. The co-added radio continuum image appeared to be unresolved with no extended emission. Therefore, the central specific intensity value was used as a measure of the total flux density. Converting from flux density to luminosity density using the cosmological distance and deredshifting the radio continuum emission from $z = 0.37$ gives an average 1.4 GHz radio continuum luminosity density of $(8.96 \pm 0.96) \times 10^{28}$ erg s^{-1} Hz^{-1} for the [O II] emission galaxies. This measurement is the large circular point in Fig. 21.

The dashed line in Fig. 21 is the 1.4 GHz radio continuum conversion to SFR (Bell 2003). There is a change in the slope of this conversion at an SFR of $\sim$3.5 M$_\odot$ yr^{-1}. This is due to galaxies of lower mass not being able to retain all their cosmic rays accelerated in supernova remnants and so reducing the radio continuum emission produced relative to other star formation indicators. The value for the [O II] emission subsample lies $\sim 1\sigma$ below this conversion line, showing reasonable agreement. The result shown here does not depend on a handful of galaxies with high radio continuum luminosity but is a general result from all the galaxies in the subsample.

There is some intrinsic scatter (i.e. not purely random error) around the SFR correlation between different indicators. The galaxies studied in the Abell 370 analysis have been selected based on their [O II] equivalent widths. This will create a selection bias such that we may miss those galaxies that have low [O II] luminosities but higher radio continuum that exist within the general scatter of the correlation. If these galaxies were included in the sample, the average [O II] SFR would slightly decrease and average radio continuum luminosity increase. This would bring the average point in Fig. 21 closer to the line derived by Bell (2003).

Many of the individual galaxies in the [O II] emission subsample will have radio continuum luminosities below the point where the SFR correlation changes slope. As we do not have individual measures of the radio continuum luminosity for these galaxies, it is not possible to correct for this. If this could be corrected, the SFR determined from the average radio continuum of the galaxies would increase slightly, which will improve the agreement between the [O II] and radio continuum SFR.

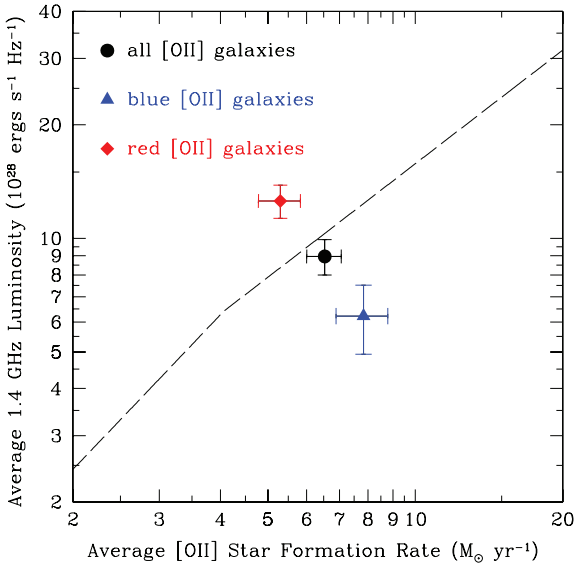

Figure 21. This figure shows the comparison of the average galaxy SFRs measured from the [O II] emission line luminosity and the deredshifted 1.4 GHz radio continuum luminosity. The dashed line is the conversion from 1.4 GHz radio continuum to SFR (Bell 2003). The large circular point is the average for all 168 galaxies with [O II] emission. The triangle point is the average for the 81 blue galaxies with [O II] emission. The diamond point is the average of the 87 red galaxies with [O II] emission.

It has been found that AGN dominate the radio continuum sources above 1.4 GHz luminosities of 10^{30} erg s^{-1} Hz^{-1} and star formation below this value (Condon, Cotton & Broderick 2002). The highest individually measurable radio continuum luminosity for a galaxy in the Abell 370 [O II] emission subsample is $(0.884 \pm 0.080) \times 10^{30}$ erg s^{-1} Hz^{-1}. This brightest radio continuum source in the [O II] emission subsample falls below this transition value with the majority of galaxies having appreciably lower radio continuum luminosities. Thus, it is likely that the AGN contamination of the sample is small with a minimal effect on the measured average radio continuum luminosity.

The [O II] emission galaxies were split into 81 blue and 87 red galaxies, and the average radio continuum luminosity and average [O II] SFRs for these subsamples were measured. In Fig. 21, the average values for the blue [O II] emission subsample are the triangular point, and the average values for the red [O II] emission subsample are the diamond point. An unexpected relationship is seen, with the red galaxies showing a higher radio continuum luminosity compared to the blue galaxies even though the red galaxies have a lower [O II] SFR. It is not known what is causing this relationship. It is not due to the effect of a small handful of galaxies in the red and blue subsamples; it is a general trend across both subsamples. No simple systematic effect, such as AGN contamination on the radio continuum, or metallicity and/or dust extinction effects on the [O II] SFR are able to explain this trend. Since the [O II] star formation–H I mass correlation seems to agree with expectations (see in Section 7.1), it is likely that the radio continuum is the cause of this unusual relationship.

A working hypothesis to explain this effect is the different timescale responsible for the production of the [O II] and radio continuum

emission in galaxies. The weak radio continuum observed in normal galaxies is emitted by an ensemble of relativistic electrons that are produced in supernova remnants. Lifetimes of these relativistic particles can exceed the time-scale associated with starbursts. The lifetime, $t_{\rm life}$, of synchrotron emitting particles capable of emitting a characteristic frequency can be expressed as

$$t_{\rm life} \sim 3\times10^4\, B^{-3/2}\, \nu_{\rm c}^{-1/2}\ {\rm yr}, \quad (4)$$

where B is the magnetic field strength of the galaxy (in G), $\nu_{\rm c}$ is the characteristic frequency of emission and can be expressed as $\nu_{\rm c} \sim 4 \times 10^6\, B\gamma^2$ Hz and γ is the electron Lorentz factor (Rybicki & Lightman 1986). For frequencies of 1 GHz, $t_{\rm life} \sim B^{-3/2}$ yr, which ranges from 3×10^7 to 10^9 years for the dilute magnetic fields (1 to 10 μG) in an ageing disc galaxy.

Thus, we suggest that red [O II] galaxies are older galaxies coming out of a burst of star formation. They have some [O II] emission left behind as well as supernova remnants that have produced a large reservoir of decaying, relativistic electrons in the galaxies. The blue [O II] galaxies are younger systems, which are only currently seen to be building their stellar populations and their relativistic electron distributions. The hypothesis is that this difference in relativistic electron distributions between the red [O II] and blue [O II] galaxies is the cause of the difference in their radio continuum measurements.

8 CONCLUSION

We have measured the average H I mass for a large sample of galaxies around the galaxy cluster Abell 370 at a redshift of $z = 0.37$, a look-back time of ∼4 billion years. The average H I mass measured for all 324 galaxies is $(6.6 \pm 3.5) \times 10^9\,{\rm M}_\odot$, while the average H I mass measured for the 105 optically blue galaxies is $(19.0 \pm 6.5) \times 10^9\,{\rm M}_\odot$. The H I gas content of the galaxies is found to be markedly higher than that found in nearby clusters. Abell 370 has considerably more H I gas than Coma, a cluster of similar size. The average galaxy H I mass measurements in Abell 370 are ∼10 times higher than similar measurements made from galaxies in Coma. The measured H I density around the galaxy cluster Abell 370 is ∼8 higher than in Coma. These results show there has been substantial evolution in the gas content of clusters over the past ∼4 billion years.

Despite the appreciable H I gas content in the Abell 370 galaxies, there is evidence that environmental effects reduce the gas content of galaxies, similar to what is seen in nearby clusters. The galaxies in the inner regions of the cluster (within the R_{200} radius) have average H I masses smaller by a factor of ∼3.5 than galaxies outside this region. The optically blue galaxies outside the hot, intracluster medium of the cluster core have a higher average H I gas mass than found from the complete sample of blue galaxies in Abell 370. This shows that the late-type galaxies close to the cluster core in Abell 370 are H I deficient like those seen in nearby clusters (Haynes et al. 1984).

Although the galaxies in Abell 370 have high H I gas contents, they have similar galaxy properties to present-day galaxies: the Abell 370 galaxies have normal H I mass-to-optical-light ratios and have a similar correlation between their SFR and H I mass as found in nearby galaxies. The average SFR derived from [O II] emission and from deredshifted 1.4 GHz radio continuum for the Abell 370 galaxies follows the correlation found in the local Universe. However, there is an unexpected relationship where the red [O II] emission galaxies have a higher average radio continuum luminosity than the blue [O II] emission galaxies despite having a lower average [O II] SFR. This effect is the reverse of what is expected and is currently unexplained.

The data suggest that the red galaxies in Abell 370 may have discernible amounts of H I gas contained within their central regions unlike nearby galaxies. Additionally, the blue galaxy population with no appreciable [O II] emission appears to contain large amounts of H I gas. Both of these results merit further investigation in future more sensitive observations.

The current rate of star formation in the Abell 370 galaxies can easily exhaust their H I gas in the ∼4 billion years to the present epoch. Abell 370 seems set to evolve into a gas-poor system like nearby galaxy clusters, especially when one considers the other physical mechanisms besides star formation that may reduce the gas content of the galaxies in the dense galaxy environment. Such a rapid rate of decrease in H I gas in the volume around Abell 370 would be significantly faster than the rate of decrease seen in field environments.

The final evolved state of the galaxy cluster Abell 370 has not been considered. This is a complex problem involving looking at the effect of the current measured SFRs in the galaxies, the effect of passive evolution on the stellar population of the galaxies, the possible growth in the cluster core mass, the motion of the galaxies in the cluster potential and the precise effects of the environment on each galaxy which will change with time as the galaxies move within the cluster.

One question that has not been answered is why Abell 370 has such a large H I gas content compared to nearby galaxy clusters. In order to produce the mass in stars seen in galaxies, it is necessary for there to be replenishment of the H I gas to fuel sufficient star formation (Hopkins et al. 2008). This replenishment must come from ionized hydrogen (H II gas) around the galaxy becoming sufficiently dense and cool to condense into H I gas which can then fuel star formation in a galaxy. At some point, this process stops in clusters so that they evolve into the H I poor systems that are seen today. There are two possible models to explain this decrease in H II condensation: the 'reservoir' model and the 'accretion' model.

In the 'reservoir' model, there is an envelope of ionized gas surrounding a galaxy that can fall on to the galaxy over time and condense into H I gas. A galaxy would slowly use up the ionized gas component of this envelope that could condense to H I gas which would eventually halt star formation in that galaxy. Interactions in higher galaxy density regions would cause galaxies to use up this envelop faster by either driving this gas into the galaxies to condense faster or removing it from the halo of the galaxies entirely (i.e. strangulation).

In the 'accretion' model, ionized gas moves from the IGM on to a galaxy where it reaches sufficient density to condense into H I gas. This accreted ionized gas would not have initially been gravitationally bound to the galaxy unlike the ionized gas in the 'reservoir' model. The expansion of the Universe with time would slow the rate at which this intergalactic ionized gas can fall on to galaxies, reducing the production of H I gas and hence the rate of star formation in the galaxies. The rate of gas replenishment in this mechanism will be proportional to the density of the intergalactic material which will be inversely proportional to the physical volume size of an element of comoving volume (the change in the size of Universe). At $z = 0.37$, the redshift of Abell 370, a comoving volume element of the Universe would have a physical volume that is ∼40 per cent its current size, a significant difference. Once the expansion of the Universe has caused this gas accretion to drop to a low level, the rate of interactions in high-galaxy-density environments would quickly use up H I gas in the galaxies creating the H I

gas-poor clusters we see today. Galaxies in lower density regions with slow SFRs would be able to retain their existing H I gas for longer.

Distinguishing between these two models is not easy as both involve ionized H II gas which is notoriously hard to measure. The best hope for understanding what is occurring will come from comparing how the SFR and H I gas content of galaxies in clusters and in lower density 'field' environments change with time.

ACKNOWLEDGMENTS

We thank the staff of the GMRT who have made these observations possible. The GMRT is run by the National Centre for Radio Astrophysics of the Tata Institute of Fundamental Research. We are grateful to the staff of the Anglo Australian Observatory and the staff of the Siding Spring Observatory for their assistance. This research was supported under Australian Research Council's Discovery Projects funding scheme (project no. 0559688). This research has made use of the GOLDMINE data base. We are indebted to Andrew Hopkins, Agris Kalnajs, Stefan Keller, Wolfgang Kerzendorf, Bruce Peterson and Eduard Westra for their valuable help.

REFERENCES

Baldwin J. A., Phillips M. M., Terlevich R., 1981, PASP, 93, 5
Balogh M. L., Schade D., Morris S. L., Yee H. K. C., Carlberg R. G., Ellington E., 1998, ApJ, 504, L75
Balogh M. L., Morris S. L., Yee H. K. C., Carlberg R. G., Ellingson E., 1999, ApJ, 527, 54
Balogh M. et al., 2004, MNRAS, 348, 1355
Basilakos S., Plionis M., Kovač K., Voglis N., 2007, MNRAS, 378, 301
Becker R. H., White R. L., Helfand D. J., 1995, ApJ, 450, 559
Bell E. F., 2003, ApJ, 586, 794
Bessell M. S., Castelli F., Plez B., 1998, A&A, 333, 231
Bravo-Alfaro H., Cayatte V., van Gorkom J. H., Balkowski C., 2000, AJ, 119, 580
Broeils A. H., Rhee M.-H., 1997, A&A, 324, 877
Butcher H., Oemler A., 1984, ApJ, 285, 426
Calzetti D., 1997, AJ, 113, 162
Carlberg R. G. et al., 1997, ApJ, 485, L13
Catinella B., Haynes M. P., Giovanelli R., Gardner J. P., Connolly A. J., 2008, ApJ, 685, L13
Cayatte V., van Gorkom J. H., Balkowski C., Kotanyi C., 1990, AJ, 100, 604
Chengalur J. N., Braun R., Wieringa M., 2001, A&A, 372, 768
Chung A., van Gorkom J. H., Kenney J. D. P., Vollmer B., 2007, ApJ, 659, L115
Condon J. J., Cotton W. D., Broderick J. J., 2002, AJ, 124, 675
Cortese L. et al., 2008, MNRAS, 383, 1519
Couch W. J., Sharples R. M., 1987, MNRAS, 229, 423
De Propris R. et al., 2003, MNRAS, 342, 725
De Propris R. et al., 2004, MNRAS, 351, 125
Diaferio A., Kauffmann G., Balogh M. L., White S. D. M., Schade D., Ellingson E., 2001, MNRAS, 323, 999
Doyle M. T., Drinkwater M. J., 2006, MNRAS, 372, 977
Dressler A., 1980, ApJ, 236, 351
Dressler A. et al., 1997, ApJ, 490, 577
Dressler A., Oemler A. J., Poggianti B. M., Smail I., Trager S., Shectman S. A., Couch W. J., Ellis R. S., 2004, ApJ, 617, 867
Farouki R., Shapiro S. L., 1981, ApJ, 243, 32
Fasano G., Poggianti B. M., Couch W. J., Bettoni D., Kjaergaard P., Moles M., 2000, ApJ, 542, 673
Gómez P. L. et al., 2003, ApJ, 584, 210
Gavazzi G., Boselli A., Donati A., Franzetti P., Scodeggio M., 2003, A&A, 400, 451
Gavazzi G., Boselli A., van Driel W., O'Neil K., 2005, A&A, 429, 439
Gavazzi G., O'Neil K., Boselli A., van Driel W., 2006, A&A, 449, 929
Gunn J. E., Gott J. R. I., 1972, ApJ, 176, 1
Hashimoto Y., Oemler A. J., Lin H., Tucker D. L., 1998, ApJ, 499, 589
Haynes M. P., Giovanelli R., Chincarini G. L., 1984, ARA&A, 22, 445
Hopkins A. M., 2004, ApJ, 615, 209
Hopkins A. M., McClure-Griffiths N. M., Gaensler B. M., 2008, ApJ, 682, L13
Kauffmann G., White S. D. M., Heckman T. M., Menard B., Brinchmann J., Charlot S., Tremonti C., Brinkmann J., 2004, MNRAS, 353, 713
Kennicutt R. C., Jr, 1983, ApJ, 272, 54
Kewley L. J., Geller M. J., Jansen R. A., 2004, AJ, 127, 2002
Kim A., Goobar A., Perlmutter S., 1996, PASP, 108, 190
Lah P. et al., 2007, MNRAS, 376, 1357
Larson R. B., Tinsley B. M., Caldwell C. N., 1980, ApJ, 237, 692
Lewis I. et al., 2002, MNRAS, 334, 673
Lilly S. J., Le Fevre O., Hammer F., Crampton D., 1996, ApJ, 460, L1
McGaugh S. S., Schombert J. M., Bothun G. D., de Blok W. J. G., 2000, ApJ, 533, L99
Madau P., Ferguson H. C., Dickinson M. E., Giavalisco M., Steidel C. C., Fruchter A., 1996, MNRAS, 283, 1388
Meyer M. J. et al., 2004, MNRAS, 350, 1195
Moore B., Katz N., Lake G., Dressler A., Oemler A., 1996, Nat, 379, 613
Moore B., Lake G., Katz N., 1998, ApJ, 495, 139
Niklas S., Klein U., Wielebinski R., 1997, A&A, 322, 19
Ota N., Mitsuda K., 2004, A&A, 428, 757
Pimbblet K. A., Smail I., Kodama T., Couch W. J., Edge A. C., Zabludoff A. I., O'Hely E., 2002, MNRAS, 331, 333
Poggianti B., 2004, in Dettmar R., Klein U., Salucci P., eds, Baryons in Dark Matter Halos. SISSA, Bologna, p. 104.1
Poggianti B. M., 1997, A&AS, 122, 399
Poggianti B. M., Smail I., Dressler A., Couch W. J., Barger A. J., Butcher H., Ellis R. S., Oemler A. J., 1999, ApJ, 518, 576
Poggianti B. M. et al., 2008, ApJ, 684, 888
Prochaska J. X., Herbert-Fort S., Wolfe A. M., 2005, ApJ, 635, 123
Quilis V., Moore B., Bower R., 2000, Sci, 288, 1617
Rao S. M., Turnshek D. A., Nestor D. B., 2006, ApJ, 636, 610
Richstone D. O., 1976, ApJ, 204, 642
Roberts M. S., Haynes M. P., 1994, ARA&A, 32, 115
Rybicki G. B., Lightman A. P., 1986, Radiative Processes in Astrophysics. Wiley-VCH, Weinheim
Schlegel D. J., Finkbeiner D. P., Davis M., 1998, ApJ, 500, 525
Schmidt B. P. et al., 1998, ApJ, 507, 46
Solanes J. M., Manrique A., Garcia-Gomez C., Gonzalez-Casado G., Giovanelli R., Haynes M. P., 2001, ApJ, 548, 97
Sullivan M., Mobasher B., Chan B., Cram L., Ellis R., Treyer M., Hopkins A., 2001, ApJ, 558, 72
Toomre A., Toomre J., 1972, ApJ, 178, 623
Verheijen M. A. W., 2004, in Diaferio A., ed., Proc. IAU Colloq. 195, Galaxy Evolution in Dense Environments: a Concise HI Perspective. Cambridge Univ. Press, Cambridge, p. 394
Verheijen M., van Gorkom J. H., Szomoru A., Dwarakanath K. S., Poggianti B. M., Schiminovich D., 2007, ApJ, 668, L9
Wieringa M. H., de Bruyn A. G., Katgert P., 1992, A&A, 256, 331
Wu X.-P., Xue Y.-J., Fang L.-Z., 1999, ApJ, 524, 22
Zwaan M. A., 2000, PhD thesis, Univ. Groningen
Zwaan M. A., Briggs F. H., Sprayberry D., Sorar E., 1997, ApJ, 490, 173
Zwaan M. A., van Dokkum P. G., Verheijen M. A. W., 2001, Sci, 293, 1800
Zwaan M. A., Meyer M. J., Staveley-Smith L., Webster R. L., 2005, MNRAS, 359, L30

This paper has been typeset from a TEX/LATEX file prepared by the author.